Early-stage hypogene karstification in a mountain hydrologic system: A coupled thermohydrochemical model incorporating buoyant convection

A. Chaudhuri,[1] H. Rajaram,[2] and H. Viswanathan[3]

[1] The early stage of hypogene karstification is investigated using a coupled thermohydrochemical model of a mountain hydrologic system, in which water enters along a water table and descends to significant depth ($\sim$1 km) before ascending through a central high-permeability fracture. The model incorporates reactive alteration driven by dissolution/ precipitation of limestone in a carbonic acid system, due to both temperature- and pressure-dependent solubility, and kinetics. Simulations were carried out for homogeneous and heterogeneous initial fracture aperture fields, using the FEHM (Finite Element Heat and Mass Transfer) code. Initially, retrograde solubility is the dominant mechanism of fracture aperture growth. As the fracture transmissivity increases, a critical Rayleigh number value is exceeded at some stage. Buoyant convection is then initiated and controls the evolution of the system thereafter. For an initially homogeneous fracture aperture field, deep well-organized buoyant convection rolls form. For initially heterogeneous aperture fields, preferential flow suppresses large buoyant convection rolls, although a large number of smaller rolls form. Even after the onset of buoyant convection, dissolution in the fracture is sustained along upward flow paths by retrograde solubility and by additional "mixing corrosion" effects closer to the surface. Aperture growth patterns in the fracture are very different from those observed in simulations of epigenic karst systems, and retain imprints of both buoyant convection and preferential flow. Both retrograde solubility and buoyant convection contribute to these differences. The paper demonstrates the potential value of coupled models as tools for understanding the evolution and behavior of hypogene karst systems.

1. Introduction

[2] Karst systems form by dissolution of soluble rocks to produce features such as caves, sinkholes, and subsurface conduit networks. Karst systems are broadly classified as epigenic (formed by the movement of water from overlying or immediately adjacent recharge surfaces, typically in unconfined settings), syngenetic (formed in young, porous carbonate rocks simultaneously as they underwent lithification, typically in coastal or oceanic settings), and hypogene (formed by water in which the dissolution power was produced at depth beneath the surface, independent of surface or soil CO_2 or other near surface acid sources) [*Ford and Williams*, 1989; *Palmer*, 1991; *Palmer and Palmer*, 2000; *Klimchouk*, 2009]. Alternative definitions of hypogene cave systems have emphasized the role of hydrothermal waters or waters containing hydrogen sulfide, or by acids of deep-seated origin, including epigenic waters whose acidity is renewed by deep-seated processes [e.g., *Ford and Williams*, 1989; *Worthington and Ford*, 1995]. *Ford* [2006] and *Klimchouk* [2009] suggest that the above alternative definitions are unified by noting that the most important common hydrogeological feature shared by hypogene karst systems is that they are formed in confined settings by flow of water into a soluble formation from below. The processes, mechanisms, and timescales associated with the origin and development of hypogene karst systems are of significant hydrogeological and speleological interest [*Palmer*, 1991; *Ford and Williams*, 2007; *Klimchouk*, 2009], and also relevant in the context of renewable geothermal energy development and subsurface carbon sequestration in deep karst systems [*Dreybrodt and Gabrovsek*, 2003; *Klimchouk*, 2007; *Goldscheider et al.*, 2010]. One subset of hypogene karst systems is formed in settings where meteoric waters circulate to great depths and rise up along high-permeability vertical or subvertical fracture/ fault zones [*Ford and Williams*, 2007; *Perry et al.*, 1979;

[1]Department of Applied Mechanics, Indian Institute of Technology Madras, Chennai, Tamil Nadu, India.
[2]Department of Civil, Environmental and Architectural Engineering, University of Colorado, Boulder, Colorado, USA.
[3]Earth and Environmental Sciences Division, Los Alamos National Laboratory, Los Alamos, New Mexico, USA.

Corresponding author: H. Rajaram, University of Colorado, Civil, Environmental, & Architectural Engineering, Engineering Center Office Tower 441, 428 UCB, Engineering Center ECOT 441, Boulder, CO 80309, USA. (hari@colorado.edu)
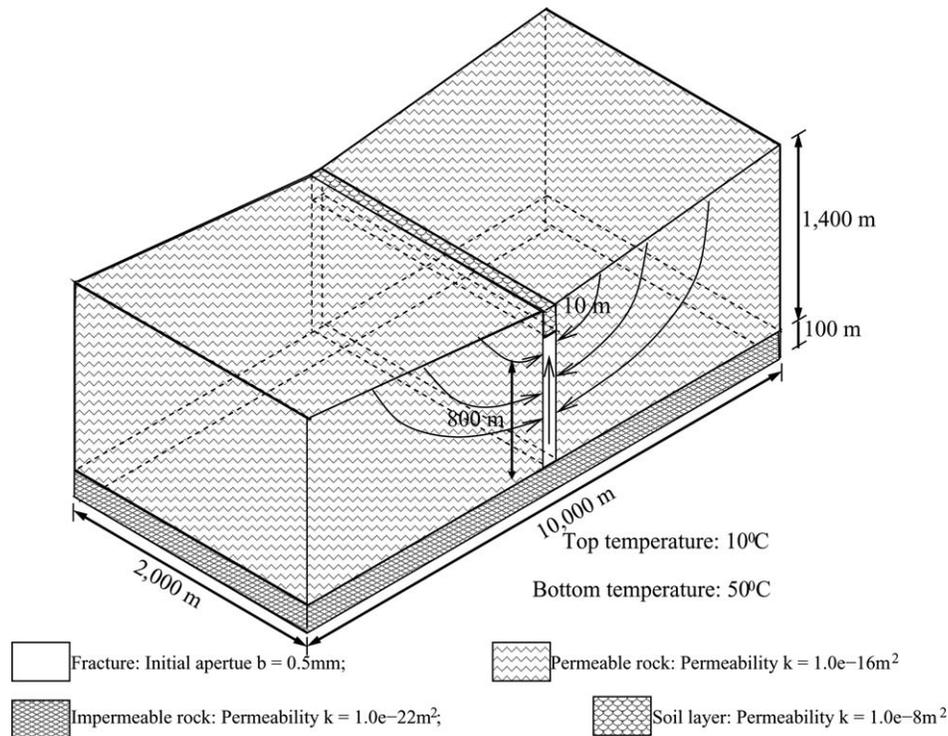
Figure 1. Geometry and dimensions of the prototype mountain hydrologic system used in our simulations. The top surface schematically shows the prescribed water table (1400 m above the impermeable rock layer at the outer boundaries, and 900 m above the impermeable rock layer in the center, with a linear increase away from the center on both sides). The temperature variation at the model boundaries was specified as a linear variation from 50°C at the bottom of the domain (45°C at the bottom of the fracture) to 10°C at the top. The Ca^{2+} concentrations were set equal to the saturation concentrations at the local temperature along these boundaries. At the water table, the Ca^{2+} concentration is assigned based on equilibrium with calcite at 10°C and a P_{CO_2} of 0.03 atm.

Hobba et al., 1979; *Severini and Huntley*, 1983; *Palmer*, 1991; *Goldscheider et al.*, 2010; *Davidson et al.*, 2011]. Examples of karst systems of this category include karst springs in the Warm springs valley anticline in northwestern Virginia and other areas within the Appalachians [*Hobba et al.*, 1979; *Serevini and Huntley*, 1983]; the Roszadomb thermal springs in Budapest, Hungary [*Ford and Williams*, 2007; *Goldscheider et al.*, 2010]; the thermal springs of Bath, England [*Andrews et al.*, 1982]; and cave systems of the southern Guadalupe mountains in New Mexico and Texas and Black Hills of South Dakota [*Palmer*, 1991; *Ford and Williams*, 2007; *Bakalowicz et al.*, 1987].

[3] Some of the important factors that facilitate karstification in hypogene systems are (i) deep circulation of water to depths (order of 1 km) where its temperature can be raised significantly (all references listed above), or cross-formational flow of warm waters from depth [*Ford*, 2006; *Klimchouk*, 2009]; (ii) the retrograde solubility of calcite, which enables karstification by cooling of upward flowing waters [*Palmer*, 1991; *Andre and Rajaram*, 2005]; (iii) mixing corrosion [*Bogli*, 1964] wherein mixtures of different calcite-saturated waters circulating to different depths produces undersaturation; (iv) high permeability in vertical or subvertical fracture or fault zones that drives rapid upward flow; and (v) groundwater containing acids such as hydrogen sulfide and sulfuric acid in addition to carbonic acid [*Palmer*, 1991; *Ford and Williams*, 2007]. Previous

efforts to develop computational models of hypogene karst systems [*Palmer*, 1991; *Andre and Rajaram*, 2005] attempted to constrain the timescales associated with hypogene karstification using simple one-dimensional models. *Andre and Rajaram* [2005] showed that the aperture of a fracture supporting upward flow in a geothermal gradient grows more or less uniformly along its length, producing a sharp increase in growth rate, aperture, and flow rate, at a characteristic time which they denoted as "maturation time." They derived analytical estimates of the maturation time, which depends on the hydraulic and geothermal gradients. For typical values of the initial fracture aperture, they showed that karstification can occur over timescales of the order of a few to tens of thousands of years. They also developed numerical models that considered both conductive and forced-convective heat transport to demonstrate that forced convection effects reduce the effectiveness of retrograde solubility by reducing the thermal gradients along the upward flow paths. However, they also suggested that a more complete model should consider the possibility of buoyant convection because it is clear that warmer lighter water is below colder heavier water in these settings. *Klimchouk* [2009] pointed out the widespread evidence for morphologies resulting from buoyant convection in hypogene karst systems. *Severini and Huntley* [1983] demonstrated that spring temperatures in the Warm Springs Valley thermal karst are consistent with a mixed forced-

free convection regime, thus implicating the influence of buoyancy effects. The importance of incorporating buoyancy driven flow in hypogene karst models is thus established. *Chaudhuri et al.* [2009] demonstrated the onset of buoyant convection in vertical fractures, once fracture aperture was enlarged above a critical value by dissolution. They also proposed a critical Rayleigh number criterion for fractures bounded by conductive rock. However, their approach did not consider the kinetics of calcite dissolution. Instead, they used the solubility gradients along the flow vectors to compute fracture aperture alteration rates, based on the "gradient-reaction" model of *Phillips* [1991]. Interactions between buoyant convection and reactive transport are also implicated in the evolution of porosity and permeability in carbonate platforms [e.g., *Jones and Xiao*, 2006].

[4] In this paper, we develop a coupled thermohydrochemical model of the early stages of hypogene or thermal karstification in a mountain hydrologic system, which considers both calcite dissolution kinetics and buoyancy effects in addition to other relevant processes and mechanisms. Our conceptualization of the mountain hydrologic system (Figure 1) is consistent with the hydrogeologic setting and probable flow systems associated with several thermal spring systems in the Appalachians [*Hobba et al.*, 1979; *Severini and Huntley*, 1983] and incorporates many of the generic features of hypogene carbonate rock environments described by *Palmer* [1991], *Ford and Williams* [2007], and *Goldscheider et al.* [2010]. Flow in this mountain hydrologic system is driven by a sloping water table in a carbonate rock matrix, intersected by a permeable fracture zone at the middle of the valley. Due to computational limitations, the central fracture zone is represented as a single fracture/"fault" plane. This is an idealization that precludes our ability to simulate the widely observed maze-like macromorphologies of hypogene caves, which largely derive from fracture network structure [*Klimchouk*, 2009]. However, our conceptual model set-up permits the development of mesomorphological features described as the "morphological suite of rising flow" by *Klimchouk* [2009]. The rock matrix on the valley slopes is represented as an equivalent porous medium rather than discretely fractured rock, again to facilitate computational tractability. Although the porosity and permeability of the rock matrix were allowed to evolve with time in the simulations, they were not significantly altered even over long timescales, as discussed below. The 1.4 km depth of the circulating flow system in Figure 1 is within the range of reported circulation depths for hypogene karst systems [*Hobba et al.*, 1979; *Palmer*, 1991; *Goldscheider et al.*, 2010; *Davidson et al.*, 2011]. A basement rock unit with low permeability is assumed to underlie the 1.4 km thick carbonate unit. The recharge areas of roughly 10 km^2 on each side of the valley are within the range of values reported by *Hobba et al.* [1979]. For simplicity, and in the interest of maintaining a tractable scope for the paper, we did not consider multiple geologic units in the system above the basement rock. We acknowledge that many of the spring systems described by *Hobba et al.* [1979] and hypogene cave systems described by *Klimchouk* [2009] involve cross-formational flow paths that cut across multiple geologic units. Our modeling approach can be extended readily to simulate karstification

in limestone units that only comprise a part of the overall stratigraphy. More details on the model set-up and boundary conditions are provided in section 2. The equations for fluid flow, heat transport, and multispecies reactive transport in the system are described in section 3. We employ a multispecies reactive transport model for the carbonic acid system. Mathematical manipulation of the geochemical system using the component method [*Morel and Hering*, 1993] reduces the system of transport equations to a single transport equation for total calcium concentration, coupled with speciation calculations. Results of the simulations are presented in section 4, and the implications of our results are discussed in section 5.

2. Conceptual Model Set-Up Boundary Conditions and Initial Aperture Fields

[5] The conceptual model set-up is shown in Figure 1, which also serves as the computational domain for the simulations presented below. The position of the water table is specified and remains fixed during the simulations. Although the water table position is known to vary in response to karstification in epigenic karst systems [*Palmer*, 1991; *Ford and Williams*, 2007; *Dreybrodt et al.*, 2005], the relatively low permeability of the rock matrix $\left(10^{-16} \mathrm{m}^2\right)$, and the fact that it does not change significantly even over long simulation times (as demonstrated below), partially justifies this boundary condition in our model for hypogene karstification. For simplicity, a linear variation with a water table slope of 0.1 was specified. The water table head is the driving head for flow in the mountain hydrologic system. An impermeable boundary was specified at the bottom of the computational domain. With these boundary conditions, water enters the domain at the water table and flows out through the central fracture. In the later stages of the simulation, after the onset of buoyant convection, there are flows both in and out of the top of the fracture due to convection rolls. A 10 m thick soil or rubble layer is specified at the top of the central fracture with a permeability of $10^{-8} \mathrm{m}^2$, which is much larger than the initial permeability of the fracture. The permeability of this layer is assumed to remain constant and is not altered by dissolution. This was done largely to avoid numerical artifacts that arose from allowing dissolution at the outflow boundary.

[6] The temperature at the bottom of the computational domain is set at 50°C and the temperature at the top in the rock matrix (i.e., at the water table) is specified as 10°C. On the outside walls of the computational domain, a linear temperature variation between 50°C and 10°C was specified, corresponding to a geothermal gradient of about 0.029°C/m. At the outflow boundary along the top of the soil/rubble layer overlying the fracture, a zero conductive flux boundary is specified in areas where there is outflow (i.e., heat flow out of the boundary occurs by advection at a rate determined by the local flow rate and water temperature), and a temperature of 10°C is specified where there is inflow. Inflow across some portions of this boundary typically occurs after the onset of buoyant convection. A linear temperature variation from 50°C at the bottom to 10°C at the top was used as the initial temperature field.

[7] For the multispecies reactive transport model, the boundary condition specified at the top of the water table is

saturation with respect to calcite and a total dissolved carbon content corresponding to equilibrium with a vadose zone P_{CO_2} of 0.03 atm, which is in the middle of the log-range of P_{CO_2} values for soils. Values up to an order of magnitude larger have been reported [*Ford and Williams*, 2007]. Within the rock, a vadose zone is considered to overlie the water table. Rain water infiltrating through the vadose zone is assumed to experience open system conditions with $P_{CO_2} = 0.03$ atm, and attain saturation with respect to calcite at a temperature of $10°C$ when it reaches the water table. Correspondingly, the total dissolved carbon and total dissolved calcium at the water table are fixed at 1.646 mm and 0.81 mm, respectively. Below the water table (i.e., within the computational domain) the rock is fully saturated with water and the system is modeled as a closed system for reactive transport calculations. We acknowledge that our simulation results may involve restrictions imposed by the assumed value of P_{CO_2} and the assumption of saturation at the water table, which are discussed further in later sections of the paper. Along the outside walls and the bottom of the domain, where the temperature is specified, the calcium concentration is set to the saturation concentration C_{sat} at the local temperature. At the top boundary, a zero diffusive flux boundary condition is specified wherever water is flowing out of the domain. Correspondingly, water that is flowing out of the top boundary has a calcium concentration equal to that in the adjacent boundary cell, while water flowing into the fracture (as occurs after the onset of buoyant convection) has a calcium concentration equal to that at the water table. For the coupled process simulations, an initial condition for species concentrations was specified based on local chemical equilibrium at the initial temperature.

[8] Three sets of simulations were carried out: one simulation with a uniform (i.e., homogeneous) initial fracture aperture or permeability field, and two cases with heterogeneous initial aperture/permeability fields. Natural fractures/faults are widely observed to exhibit scale-dependent aperture/permeability variations [*Adler and Thovert*, 1999]; however, there are few precise observations of heterogeneity in vertical faults/fractures to guide representations of heterogeneity in our simulations. For this reason, the simulations in heterogeneous initial aperture fields are presented mainly to illustrate the potential influence of initial heterogeneity, and contrast this behavior with the highly idealized case of an initially homogeneous aperture field. We acknowledge that the values used below for the correlation lengths may be a bit on the high side. For the initially homogeneous aperture case, a value of 0.5 mm was used for the initial aperture. The initial aperture field for both heterogeneous cases is modeled as a log normal random field with the same hydraulic aperture, $b_h = 0.5$mm (this is achieved by using the same value of the mean log-aperture in all cases [*Gelhar*, 1993]) to ensure that the mean water flux (and total flow rate) through the system is the same in all cases. Because the dissolution rate during the very early stages (conductive heat transfer regime) depends strongly on the mean water flux, comparisons across different simulations will not be consistent unless the mean flow rate is initially the same across all cases simulated. The spatial correlation function of the initial log-aperture field ($\rho(\xi, \zeta)$, where ξ and ζ are respectively the separation distances in horizontal and vertical directions) for the two heterogeneous cases was specified as a Gaussian correlation function:

$$\rho(\xi, \zeta) = \exp\left(-\left(\frac{\xi}{\lambda_x}\right)^2 - \left(\frac{\zeta}{\lambda_z}\right)^2\right) \qquad (1)$$

[9] Parameter values for the two heterogeneous cases, that is, standard deviation ($\sigma_{\ln(b)}$) and correlation lengths (λ_x and λ_z), were assigned as follows:

[10] Case 1: $\sigma_{\ln(b)} = 0.85$ and correlation lengths, $\lambda_x = 60$m and $\lambda_z = 60$m,

[11] Case 2: $\sigma_{\ln(b)} = 0.46$ and correlation lengths, $\lambda_x = 120$m and $\lambda_z = 120$m,

[12] The motivation for simulating behavior in both initially homogeneous and heterogeneous aperture fields stems from previous work demonstrating the influence of heterogeneity on buoyant convection. *Lopez and Smith* [1995, 1996] modeled flow in a mountain hydrologic system (in the absence of reactive alteration) and showed that channeling (preferential flow) induced by heterogeneity breaks the systematic patterns of buoyant convection that arise in relatively homogeneous permeability fields. *Rajaram et al.* [2009] considered the interaction between buoyant convection and reactive alteration in heterogeneous initial aperture fields using a simplified model ignoring reaction kinetics. *Andre and Rajaram* [2005] and *Chaudhuri et al.* [2008] quantified the influence of heterogeneity on reactive alteration in the presence of solubility gradients in a conductive heat transfer regime. *Andre and Rajaram* [2005] and *Chaudhuri et al.* [2008] also showed that dissolution during the early-time regime before onset of buoyant convection produces preferential aperture growth and highly channelized flow. If and when there is an onset of buoyant convection in the heterogeneous fracture permeability fields, the roll pattern will be strongly influenced by the imprint of initial channelization. Thus, the behavior obtained with heterogeneous initial aperture/permeability fields is expected to differ significantly from the behavior in initially homogeneous aperture fields. Only two cases of heterogeneous initial aperture fields were simulated because numerical simulations in heterogeneous permeability fields are rather time-consuming and because of the slow convergence of iterative solvers used in the software package FEHM (Finite Element for Heat and Mass Transfer) (http://fehm.lanl.gov/ [*Zyvoloski*, 2007]). For both cases, simulations were executed for a run-time of 45 days (on an Intel Xeon E5620 processor). The simulations represent behavior over physical timescales of the order of several thousand years, thus capturing the early stages of development of the karst system by permeability growth. The time-consuming nature of the simulations also precluded detailed sensitivity analyses based on multiple simulations.

3. Governing Equations

[13] In this section, the partial differential equations for the different physical and chemical processes involved in the coupled thermohydrochemical model are described, and the nonlinear coupling among various processes is also explained.

3.1. Flow and Heat Transport Equations

[14] Flow within the fracture plane is modeled using a 2-D aperture-integrated equation. The continuity equation and the modified form of the local cubic law to express the aperture-integrated flux ($\mathbf{Q}_f$, in m^2/s) in terms of gradient of aperture-averaged pressure (P_f in MPa) are given as follows:

$$\nabla \cdot \mathbf{Q}_f = f_Q \text{ and } \mathbf{Q}_f = -\frac{b^3}{12\mu(1 + 0.00838\text{Re})}\left(\nabla P_f - \rho\mathbf{g}\right) = 0 \quad (2)$$

[15] Here f_Q is total lateral water flux entering the fracture from both sides of the low-permeability rock matrix; b, ρ, μ, P_f, and $\mathbf{g}$ are the aperture, density, dynamic viscosity, fluid pressure, and gravitational acceleration vector, respectively. The density is allowed to vary with temperature by coupling with the heat transport equation as described below, and this coupling plays an important role in generating buoyancy-driven flow. The Reynolds number is defined as ($\text{Re} = |Q_f|\rho/\mu$). At low (Re), equation (2) is equivalent to the local cubic law. To account for the reduced effective permeability due to nonlinear resistance during turbulent flow at high Re, the flux given by the local cubic law is divided by a factor $(1 + 0.00838\text{Re})$, following the experimental studies of *Zimmerman* [2004]. At high Re ($> \sim 2000$), equation (2) reduces to a fully turbulent resistance equation. As described further below, the aperture $b(x, z, t)$ grows during karstification, producing changes in the flow regime. Non-Darcian flow conditions are typically encountered after sufficient aperture enlargement and associated increase in fracture transmissivity. The flow equation (2) captures the influence of evolving aperture on the flow regime consistently, and also allows for turbulent and laminar flow in different portions of the fracture.

[16] As noted above, although the mountainside should ideally be represented as a fractured rock mass, it is modeled as an equivalent porous medium to facilitate computational efficiency. The governing equations for flow, 3-D continuity, and Darcy's equation in the rock matrix are given as follows:

$$\nabla \cdot \mathbf{q}_r = 0 \quad \text{and} \quad \mathbf{q}_r = -\frac{k}{\mu}\left(\nabla P_r - \rho\mathbf{g}\right) \quad (3)$$

where $\mathbf{q}_r, P_r$ and k are, respectively, the Darcy flux, fluid pressure, and intrinsic permeability in the rock. The interaction between flow in the rock and the fracture is taken into account using water flux and pressure boundary conditions at the fracture-rock interface. The mathematical representations of these interface conditions are as follows:

$$f_Q = q_{ry}|_{y=-b/2} - q_{ry}|_{y=b/2} \quad (4)$$

$$P_r|_{y=b/2} = P_r|_{y=-b/2} = P_f \quad (5)$$

[17] Because the behavior in the porous rock on either side of the fracture is almost identical, equation (4) implies that $f_Q(x, z, t)$ is twice the flux entering the fracture from each side of the porous rock matrix. The distribution of temperature (T in °C) in the computational domain is obtained by solving convective-diffusive heat transport equations for both fracture and rock simultaneously. Heat transport in fracture and rock are modeled using 2-D aperture-integrated and 3-D convective-diffusive heat transport equations, respectively:

$$b\frac{\partial\left((\rho C_p)_f T_f\right)}{\partial t} + \mathbf{Q}_f \cdot \nabla h_f - b\nabla \cdot \left(\lambda_f \nabla T_f\right) = f_T \quad (6)$$

$$\frac{\partial\left((\rho C_p)_r T_r\right)}{\partial t} + \mathbf{q}_r \cdot \nabla h_r - \nabla(\lambda_r \nabla T_r) = 0 \quad (7)$$

where subscript f and r, respectively, correspond to fracture and rock. In equations (6) and (7), T, C_p, h, and λ are, respectively, the temperature, specific heat capacity, enthalpy, and thermal conductivity. For the fracture, the temperature and enthalpy are aperture-averaged values. In the porous medium, the specific heat capacity and thermal conductivity are bulk porous medium values. For limestone, the values of specific heat capacity and thermal conductivity are, respectively, taken as 1000 J/kg/°C and 2.5 W/m/°C. These values are within the range given by *Robertson* [1988]. Similar to the fracture-rock interface conditions for flow, the coupling between heat transport in the fracture and rock occurs through the lateral heat exchange term $(f_T(x, z, t))$ in equation (6), which is defined by the following interface boundary conditions:

$$f_T(x, z, t) = \left(q_{ry}h_r - \lambda_r\frac{\partial T_r}{\partial y}\right)_{y=-b/2} - \left(q_{ry}h_r - \lambda_r\frac{\partial T_r}{\partial y}\right)_{y=b/2} \quad (8)$$

$$T_r|_{y=b/2} = T_r|_{y=-b/2} = T_f \quad (9)$$

[18] The convective heat transfer term in equations (6) and (7) and the temperature-dependent density and viscosity in equations (2) and (3) lead to nonlinear coupling between the heat transfer and the flow equations [*Nield and Bejan*, 2006]. The computations employ equations of state for density, viscosity, and enthalpy. These are computed as polynomial functions of temperature and pressure, following the approach used FEHM. The temperature dependence of the density plays an important role in generating buoyant convection as the fracture permeability grows.

3.2. Multispecies Reactive Transport Model

[19] Modeling dissolution/precipitation and associated aperture/porosity alteration in the mountain hydrologic system (shown in Figure 1) in general requires solution of multispecies transport equations for the species in a carbonic acid system. Due to the temperature gradients in the system, dissolution and precipitation are expected to occur in different regions. Our modeling approach accounts for the temperature-dependence of both the solubility and dissolution/precipitation kinetics of calcite. Additionally, the pressure dependence of solubility is also considered. The relevant aqueous species that control the dissolution/precipitation rates of calcite are $\{H^+, Ca^{2+}, CaHCO_3^+, OH^-, CO_3^{2-}, HCO_3^-, H_2CO_3^*, CaCO_3^*(Aq)\}$. The Tableaux method [*Morel and Hering*, 1993], with

$\left\{ \mathrm{H^+, Ca^{2+}, HCO_3^-} \right\}$ as basis species leads to the following three components:

$$TOTH = [\mathrm{H^+}] - [\mathrm{OH^-}] + [\mathrm{H_2CO_3^*}] - [\mathrm{CO_3^{2-}}] - [\mathrm{CaCO_3^*}]$$
$$TOTC = [\mathrm{CO_3^{2-}}] + [\mathrm{HCO_3^-}] + [\mathrm{H_2CO_3^*}] + [\mathrm{CaHCO_3^+}] + [\mathrm{CaCO_3^*}]$$
$$TOTCa = [\mathrm{Ca^{2+}}] + [\mathrm{CaHCO_3^+}] + [\mathrm{CaCO_3^*}] \tag{10}$$

[20] Because linear combinations of components are also valid components, we choose total charge = TOTH − TOTC + 2TOTCa and TOTC − TOTCa as components. The advantage of choosing these two quantities as components is that they are invariant in a closed chemical system. Total charge is zero everywhere. For the assumed boundary conditions at the inflow, TOTC − TOTCa is constant everywhere, equal to its constant value (0.836 mm, derived from the values of 1.646 mm for TOTC and 0.81 mm for TOTCa) at the inflow boundary because each mole of calcite dissolved/precipitated adds/removes one mole each of TOTC and TOTCa. Thus, only one transport equation (that for TOTCa) needs to be solved to model the system. However, calculation of dissolution/precipitation rates requires concentrations of all species (see equation (A1)), which need to be determined by solving the algebraic equations resulting from mass action laws for the aqueous reactions, given local values for the component concentrations. To overcome the computational effort associated with the speciation calculation, which needs to be performed at each computational node in each time step, we developed approximations to the widely used Plummer-Wigley Parkhurst (PWP) reaction rate [*Plummer et al.*, 1978] that only depend on TOTCa, temperature, and pressure, as described in detail in Appendix A. These approximations were derived by using the PWP rate to calculate dissolution/precipitation rates for a wide range of chemical conditions, and fitting the calculated rates using polynomial functions of temperature and the degree of saturation, and are shown in Appendix Figure A2.

[21] The 2-D aperture-integrated transport equation for the fracture and 3-D transport equation for the rock are given below, with C_f and C_r denoting TOTCa concentrations (molal or moles/kg of water) in the fracture and rock matrix:

$$b\frac{\partial\left(\rho_f C_f\right)}{\partial t} + \mathbf{Q}_f \cdot \nabla\left(\rho_f C_f\right) - b\nabla \cdot \left(D\nabla\left(\rho_f C_f\right)\right) = R_c + f_C \tag{11}$$

$$\frac{\partial\left(\phi\rho_f C_r\right)}{\partial t} + \mathbf{q}_r \cdot \nabla\left(\rho_f C_r\right) - \nabla \cdot \left(D\nabla\left(\rho_f C_r\right)\right) = R_c A_s \tag{12}$$

[22] Here R_c (in moles/m²/s) is the effective reaction rate for dissolution/precipitation and A_s is the equivalent specific surface area (m^{-1}) for the porous rock matrix. The dispersion coefficient, D is considered to be due to molecular diffusion only and its value is taken as $1 \times 10^{-9}\mathrm{m^2/s}$. In the fracture, the effective reaction rate is influenced by both surface reaction kinetics and diffusion of species to/from the fracture wall. Similar to the flow and thermal interactions between the fracture and rock at the fracture-rock interface (equations (2) and (6)), a lateral source term $f_C(x, z, t)$ is added to equation (11), to represent influx of
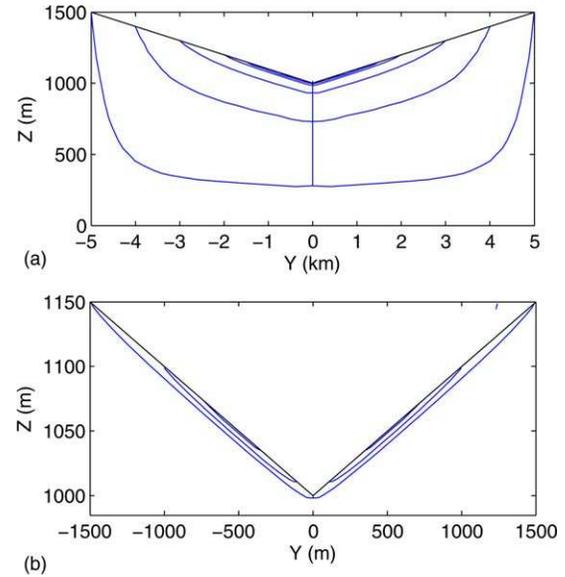
Figure 2. Streamlines showing the lateral flow from the rock matrix to the fracture: (a) streamlines in entire *y-z* plane and (b) streamlines in the vicinity of the outlet zone.

TOTCa at the fracture-rock interface, which includes TOTCa delivered by the flow across the interface from the rock to the fracture. The mathematical representations of the lateral solute flux and concentration boundary conditions at the fracture-rock interface are as given as follows:

$$f_C(x,z,t) = \left(q_{ry}C_f - D\frac{\partial C_r}{\partial y}\right)_{y=-b/2} - \left(q_{ry}C_f - D\frac{\partial C_r}{\partial y}\right)_{y=b/2} \tag{13}$$

$$C_r|_{y=b/2} = C_r|_{y=-b/2} = C_f \tag{14}$$

[23] The effective reaction rate R_c is calculated as follows:

[24] (i) For surface reaction kinetics, R_c is the PWP reaction rate denoted as R_{PWP}, modified to incorporate inhibition effects as described below. The calculation of PWP reaction rate is discussed further in Appendix A. The inhibition of the dissolution rate near saturation due to impurities adsorbed onto the surface is incorporated following the model proposed by *Svensson and Dreybrodt* [1992], leading to the modified surface reaction rate:

$$R_s = (1 - \theta)R_{\mathrm{PWP}} \tag{15}$$

where θ is the inhibition factor. *Svensson and Dreybrodt* [1992] proposed an empirical relation for θ to be calculated from concentration of calcium ion ($\{\mathrm{Ca^{2+}}\}$), which was used by *Andre et al.* [2005] in a numerical model of hypogene karstification. Because $\{\mathrm{CaHCO_3^+}\}$ and $\{\mathrm{CaCO_3^*(Aq)}\}$ are also incorporated in the geochemical model used here, TOTCa is used in place of concentration of $\{\mathrm{Ca^{2+}}\}$ in the following inhibition relation:

$$\mathrm{TOTCa} = \frac{\theta}{1 - \theta}\exp(-A - B\theta) \tag{16}$$

[25] Because the $\{\mathrm{CaHCO_3^+}\}$ and $\{\mathrm{CaCO_3^*(Aq)}\}$ concentrations are quite small, and limited data are available

on the A and B parameters in the inhibition function, we have used $A = 5.1$ for $P_{CO_2} = 0.03$ atm and $B = 2.9$ from *Andre and Rajaram* [2005]. To simplify the computation of θ from TOTCa, the following polynomial is fitted to (16) and implemented in the reactive transport model:

$$\theta = 3.35 \times 10^{-1} - 7.53 \times 10^2 (\text{TOTCa}) + 8.31 \times 10^5 (\text{TOTCa})^2 - 1.57 \times 10^8 (\text{TOTCa})^3$$

(17)

[26] (ii) The diffusion limited rate (R_d) is computed from mass transfer theory

$$R_d = \frac{\rho_f D_m S_h}{d_h} (C_{\text{sat}} - C)$$

(18)

where S_h, D_m, and d_h are the Sherwood number, molecular diffusion coefficient, and hydraulic depth, respectively. The effective value of R_c is controlled by the smaller of $\{R_s, R_d\}$. To provide a smooth variation of R_c as the aperture grows, we calculate it using the harmonic average, which is equivalent to the experimentally verified combined rate expression used by *Detwiler and Rajaram* [2007].

$$R_c = 2 \left(\frac{1}{R_s} + \frac{1}{R_d} \right)^{-1}$$

(19)

[27] In general, R_c is close to R_s for smaller values of the hydraulic depth (R_d is much larger than R_s), and closer to R_d when hydraulic depth is large (R_d is much smaller than R_s). In the porous rock matrix, R_d is very large because the pore diameters are small. Hence, we use $R_c = R_s$ in the porous rock matrix.

[28] As noted previously, the assumed boundary conditions at the water table (the P_{CO_2} value above the water table and the assumption of saturation at the water table) will influence the simulation results. However, we note that the PWP reaction rate varies only by one order of magnitude for the range of P_{CO_2}, from 0.3 atm to 0.003 atm. Furthermore, when the dissolved mineral is close to the solubility, the R_s rate is further modified by inhibition effects and our calculations revealed that the R_s rate was only 1.5 times faster when the PWP reaction rate was 10 times larger. Thus, we believe that the dissolution/precipitation rates below the water table are only slightly affected by the assumed P_{CO_2} value above the water table. On the other hand, the assumption of saturation with respect to calcite (i.e., chemical equilibrium) in formulating the boundary conditions at the water table for the closed system reactive transport calculations in the mountain hydrologic system may be more restrictive. Supersaturation is often observed in karst waters [e.g., *Ford and Williams*, 2007; *Gulley et al.*, 2013a], and may influence dissolution/precipitation rates near the water table in the rock matrix and fracture to a greater extent.

3.3. Alteration of Porosity and Permeability

[29] The local aperture and porosity alteration rates are related to the reaction rate R_c in transport equations (11)

and (12). For the fracture, the aperture alteration rate is given as follows:

$$\frac{\partial b}{\partial t} = \frac{R_c}{\rho_r \omega}$$

(20)

where $\rho_r \omega$ is molar density (in moles/m^3 = kg/m^3·moles/kg). For calcite, the number of moles of TOTCa per kg of rock is $\omega = 10$, and the density is $\rho_r = 2500$kg/m^3. The local fracture permeability also evolves with time in response to aperture alteration, and it is calculated as $k = b^2/12$. In the porous rock matrix, the porosity (ϕ) alteration rate is given as:

$$\frac{\partial \phi}{\partial t} = \frac{R_c A_s}{\rho_r \omega}$$

(21)

[30] The Kozeny-Carman equation [*Bear* 1972] was used to represent the porosity-permeability relationship and calculate the evolving permeability field due to dissolution/precipitation:

$$k = k_0 \left(\frac{\phi}{\phi_0} \right)^3 \left(\frac{1 - \phi_0}{1 - \phi} \right)^2$$

(22)

[31] Here k_0 and ϕ_0 are, respectively, the initial permeability and porosity of the porous rock.

[32] The specific surface area (A_s) also changes with time as the size of the pores and grains change due to dissolution/precipitation of minerals, a relationship that is poorly understood. We used a relationship between A_s and ϕ, presented by *Koponen et al.* [1997]:

$$A_s = A_0 \left(\frac{\phi}{\phi_0} \right) \left(\frac{\log(\phi)}{\log(\phi_0)} \right)$$

(23)

[33] The value of the reference-specific surface A_0 is taken as 65m^{-1}. However, the overall behavior of the coupled thermohydrochemical system is relatively insensitive to the A_s versus ϕ relationship, because of the small rates of alteration of the porous rock matrix, as discussed below.

3.4. Computational Implementation

[34] The transient solutions of the coupled flow (equations (1) and (2)), heat transfer (equations (3) and (4)), and solute transport (equations (8) and (9)) equations are obtained numerically by using FEHM. The capabilities of FEHM for simulating transitions of heat transfer regimes in a system with time-evolving permeability were demonstrated by *Chaudhuri et al.* [2009]. Multispecies reactive solute transport has been modeled with either explicit or implicit coupling to fluid flow and heat transport in previous work [*Robinson et al.*, 2000; *Viswanathan et al.*, 2009]. We enhanced the capabilities of FEHM by incorporating porosity-permeability alteration by dissolution/precipitation of calcite, and adapted FEHM to simulate fracture/fault permeability. The alteration of porosity-permeability is explicitly coupled with other processes for computational efficiency. The explicit coupling works satisfactorily, as the alteration rate is very slow, and thus very
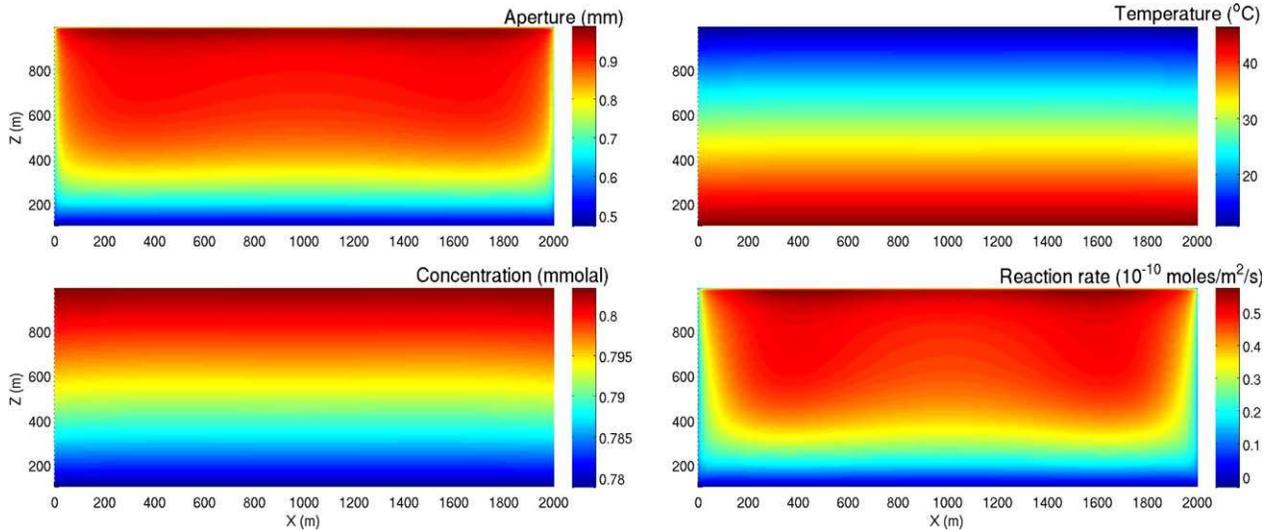
Figure 3. Initially homogeneous aperture field case: aperture, temperature, total calcium, and reaction rate fields at $t = 4280$ years. The initial aperture was constant $= 0.5$ mm everywhere in the fracture, and the initial temperature field involved a linear variation from $45°$ at the bottom to $10°$ at the top of the fracture. The minor edge effects are due to boundary conditions.

small changes occur during the typical time steps used for solving the transient flow, heat transfer, and solute transport equations.

[35] FEHM was originally developed for 3-D porous media. For a fracture plane, the various physical processes are governed by the 2-D aperture-integrated equations (equations (2), (6), and (11)). However, FEHM can be adapted to simulate the behavior of a fracture plane by representing the fracture as a thin porous layer (with geometric thickness b_p in the FEHM grid), whose flow, heat, and solute transport properties are defined so that the fracture flow, heat, and solute transport equations (2), (6), and (11) are satisfied. For example, the porosity and permeability of the "thin porous layer" used to represent the fracture are specified so that the total amount of fluid stored in fracture and transmissivity of the fracture are consistent with equation (2):

$$k = \frac{b^3}{12b_p}, \phi = \frac{b}{b_p} \qquad (24)$$

[36] For modeling heat transport through the "thin porous layer" corresponding to the fracture, the heat capacity and thermal conductivity are calculated by excluding the contribution of solid phase of the porous medium. For solute transport, the solid grains of the "thin porous layer" are considered chemically inert and to ensure the dissolution/precipitation takes place at the fracture wall, the specific surface area is taken as follows:

$$A_s = \frac{2}{b_p}, \qquad (25)$$

[37] These definitions ensure that when integrated across the thickness of the grid elements in FEHM (b_p), equations (2), (6), and (11) are satisfied. Thus, the computational domain in FEHM is composed of two different porous media. The high-permeability vertical "thin porous layer" corresponding to the fracture zone is sandwiched between two low-permeability porous media representing the rock matrix on the mountainsides. The evolution of flow and transport properties in these two media also follows different rules, consistently representing the behavior of fracture and rock defined in sections 3.1 to 3.3. The lateral flux terms that couple the flow, heat, and mass transport in the fracture and rock (equations (4), (8), and (13)) are automatically taken into account when the entire domain is modeled as a heterogeneous porous medium, and thus do not need to be specified explicitly.

4. Computational Results

[38] In this section, we present simulation results for the three cases described in section 2: initially homogeneous and two initially heterogeneous aperture/permeability fields within the central fracture zone. Our focus is on demonstrating the behavior resulting from the coupling between fluid flow, heat transfer, and reactive transport, including the influence of kinetic dissolution/precipitation. An important feature of the mountain hydrologic system in Figure 1 is that the alteration rate of the rock matrix on the mountain sides is very slow because of the low hydrologic fluxes. Most of the alteration occurs in the fracture zone, where upward flow is focused; fluid fluxes in the fracture zone are relatively large because they are fed by all the descending flow from the water table through the mountain sides (see Figure 2, showing streamlines in the y-z plane). The upward flux (Q_{fz}) increases with elevation in the fracture zone due to lateral inflow from the rock matrix. Due to the temperature gradient, water flowing upward along the fracture zone initially experiences cooling, and dissolution may be expected due to the retrograde solubility. Also, as warmer water flowing within the fracture mixes with cooler water flowing into the fracture at shallow depths, "mixing
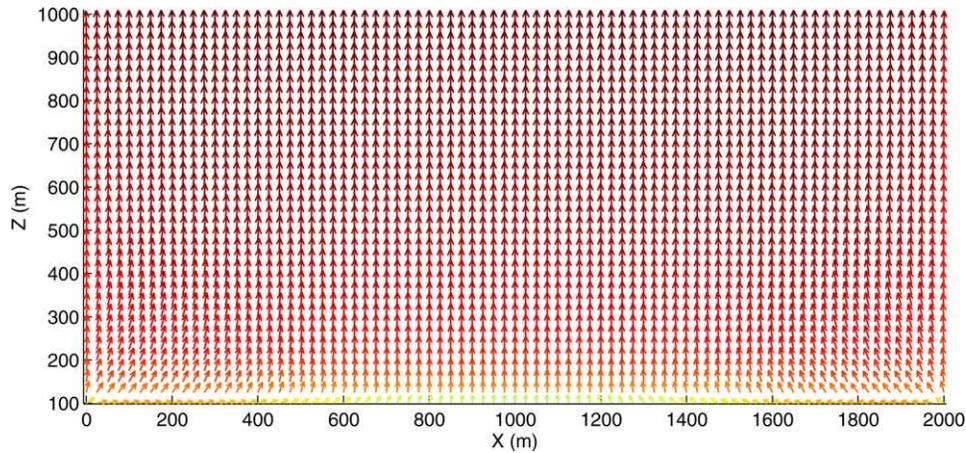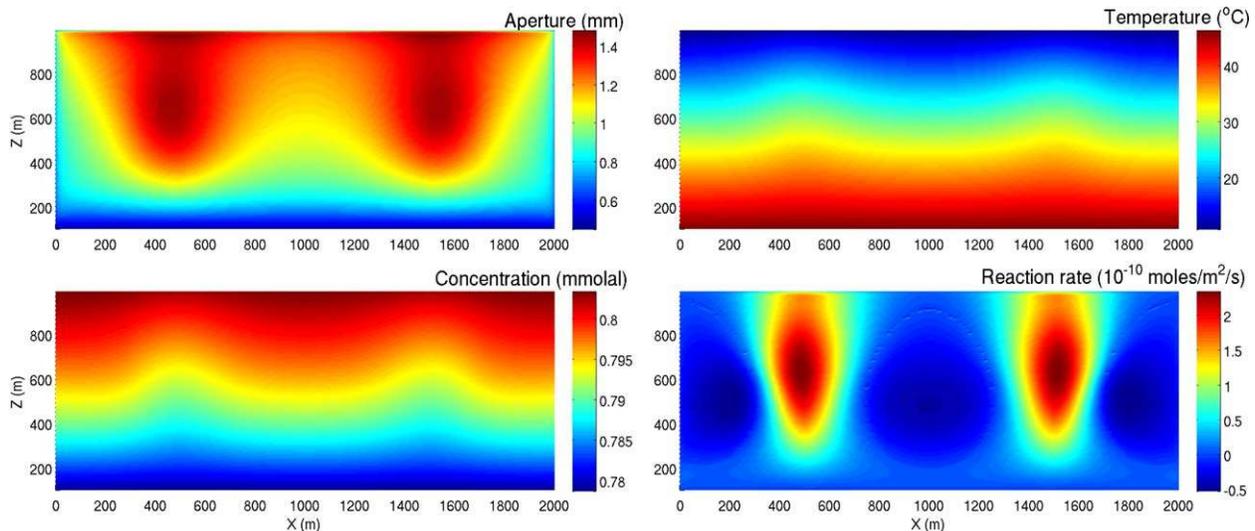
Figure 4. Initially homogeneous aperture field case: the aperture-integrated water flux vector field $\mathbf{Q}_f$ (magnitude is in log scale) at $t = 4280$ years.

corrosion" [*Bakalowicz et al.*, 1987] may be expected, and our mathematical formulation of reactive transport inherently accommodates this process by using consistent mass balance equations and reaction kinetics. In the downward flow zones in the mountain sides, slow precipitation may be expected by a combination of kinetics and solubility gradient. However, the corresponding rates of alteration are very slow, as noted above. An increase in the permeability within the fracture zone produces favorable conditions for buoyant convection rolls to form, initiating a sequence of changes in the flow, temperature, and concentration fields, as discussed below.
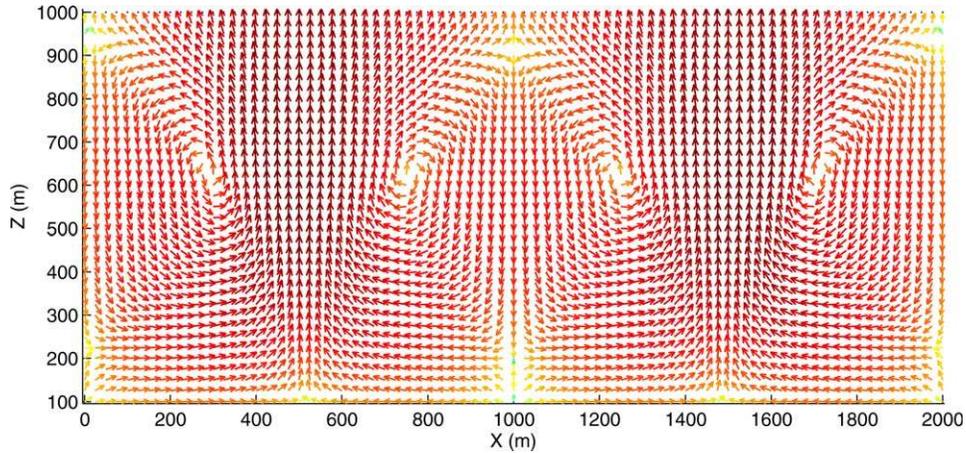
4.1. Homogeneous Initial Aperture Field

[39] For this simulation, the initial fracture aperture was assigned a uniform value of 0.5 mm over the entire fracture plane. In the early stage of aperture evolution (between 0 and approximately 4000 years), the temperature field is largely conduction-dominated and remains more or less constant at the initial geothermal gradient. Figure 3 shows the variation of aperture (b), temperature (T), TOTCa concentration (C), and reaction rates (R_C) within the fracture at 4280 years, which is representative of behavior in this early stage. Minor advective effects are discernible near the outflow boundary at the top of the fracture in the temperature plot. It is also pertinent to note that $(C_f) \approx (C_{\text{sat}}(T, P))$ (see equation (A4)) in this early stage and dissolution is driven largely by solubility gradients. The reaction rate in the fracture is positive everywhere (positive reaction rates represent dissolution), and increases with elevation, because the magnitude of the local flux (or equivalently the vertical component of the flux Q_{fz}, as the flow is largely vertical at this stage) increases with elevation within the fracture due to lateral inflow from the rock matrix (see also Figure 4, which shows a vector plot of $\mathbf{Q}_f$). The nonlinear nature of the reaction rate variation is due to both the increasing vertical flux with elevation and the nonlinear variation of solubility with temperature, and results in a nonlinear variation of aperture with elevation. The aperture growth rate does not vary significantly across the horizontal

Figure 5. Initially homogeneous aperture field case: aperture, temperature, total calcium, and reaction rate fields at $t = 7900$ years.
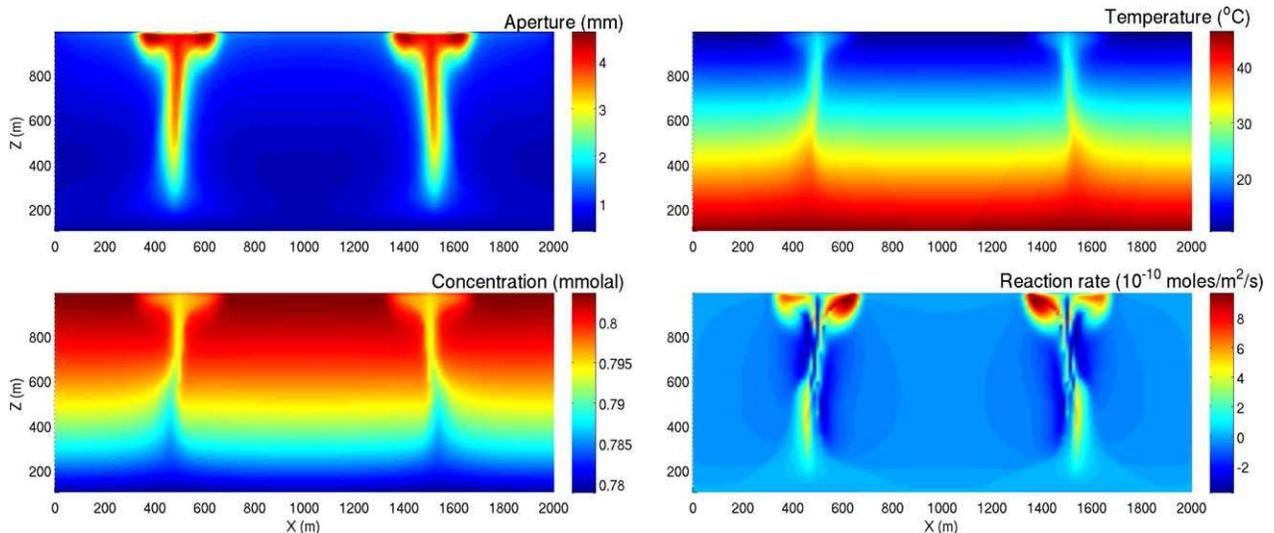
Figure 6. Initially homogeneous aperture field case: the aperture-integrated water flux vector field $\mathbf{Q}_f$ (magnitude is in log scale) at $t = 7900$ years.

direction. The increase in either the local flux $\mathbf{Q}_f$ or total outflow rate from the fracture in this early stage is insignificant, because the low rock matrix permeability controls the overall effective permeability of the mountain hydrologic system and the water table position is fixed. At 4280 years, the aperture at the top of the fracture has nearly doubled compared with the initial value.

[40] In principle, the increase in fluid temperature with depth in the fracture can result in a thermal instability and buoyant convection. However, in the very early stages, the low initial permeability and heat loss during upward advective flow by heat exchange with the rock act to stabilize the system [*Murphy*, 1979; *Chaudhuri et al.*, 2009]. With continued aperture and associated permeability/transmissivity growth, buoyancy effects can no longer be suppressed and buoyant convection rolls form at approximately 7000 years in this simulation. *Chaudhuri et al.* [2009] describe the nature of the thermal instability in a similar system (with no lateral inflow from the porous rock matrix) in detail; we relate our results to the stability criteria proposed in that

work in section 4.1.1. Figure 5 shows the aperture, temperature, concentration, and reaction rate fields at 7900 years, which is representative of behavior after the onset of buoyant convection. Figure 6 shows the corresponding vector plot of $\mathbf{Q}_f$. The behavior in this stage is mixed convective, in the sense that buoyant convection rolls are superimposed on a mean upward flow (this stage was also termed as "steady convective regime" by *Lopez and Smith* [1995], to distinguish it from an unsteady to chaotic convective regime). There are four rolls feeding two dominant upward flow paths. The most important feature of the behavior in this stage is the downward flow associated with the convection rolls in some regions of the fracture, which constitutes a reversal from the initial flow direction. The temperature and concentration fields exhibit a waviness that is consistent with the advective flow field (as shown by the $\mathbf{Q}_f$ vector plot in Figure 6). At a fixed depth, higher temperatures and lower concentrations are observed in the upward flow regions; lower temperatures and higher concentrations in the downward flow regions. The reaction rate is no longer

Figure 7. Initially homogeneous aperture field case: aperture, temperature, total calcium, and reaction rate fields at $t = 14,200$ years.
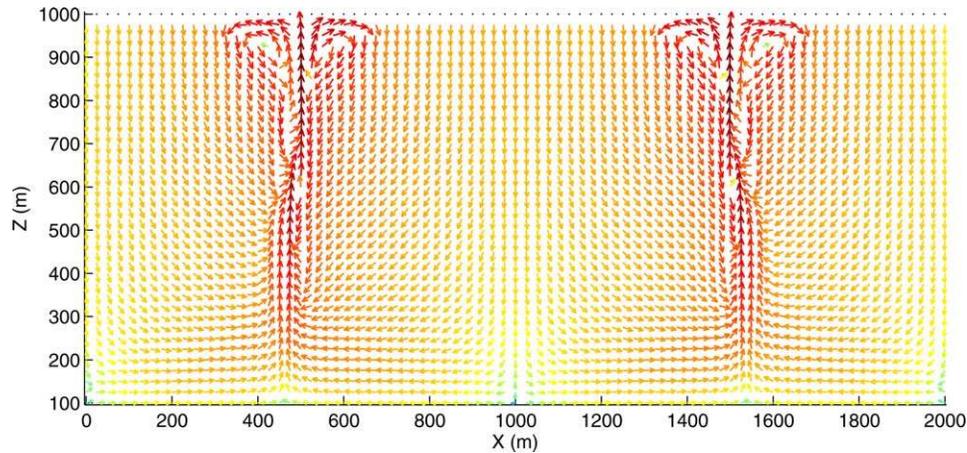
Figure 8. Initially homogeneous aperture field case: the aperture-integrated water flux vector field $\mathbf{Q}_f$ (magnitude is in log scale) at $t = 14,200$ years.

positive everywhere in the fracture. It is positive (i.e., dissolution occurs) in the upward flow regions, where water cools (solubility increases) along the flow direction, and negative (i.e., precipitation occurs) in the downward flow regions where water warms (solubility decreases) along the flow direction. The reaction rates in this stage are controlled by both solubility gradients and reaction kinetics. Correspondingly, the largest apertures are seen in the regions with high dissolution rates (i.e., along the upward flow limbs of the convection cells). The upward flow region at the center of the fracture near the outflow boundary experiences lower upward flow rates and hence lower dissolution rates. The geometry of the convection rolls at this stage are influenced by heat exchange between the fracture and porous rock [*Murphy*, 1979], the aspect ratio of the fracture, and the systematic aperture variations resulting from aperture alteration up to this point. We would expect that more buoyant convection rolls would form in a system with a larger aspect ratio (i.e., greater length in the y-direction than in the z-direction; in our simulations, the ratio of

the fracture length in the y and z directions is 10/7, see Figure 1). The pattern of buoyant convection continues to evolve as the fracture aperture and permeability increase. With time, the upward flow channels become narrower, and the downward flow regions become wider. This occurs in part because the overall water mass flux into the fracture zone remains relatively constant, and the increasing local upward fluxes in the large-aperture upward flow channels need to be supplied by descending flow over increasingly larger regions [*Rajaram et al.*, 2009].

[41] Figure 7 shows the aperture, temperature, concentration, and reaction rate fields at 14,200 years, and Figure 8 shows the corresponding $\mathbf{Q}_f$ field. An unusual pattern of convection rolls has resulted due to complex feedbacks between aperture alteration by reaction, and by regulation of the thermal instability by heat exchange with the rock matrix. *Murphy* [1979] discusses conditions under which narrow rolls form. The roll pattern involves a double-roll, with shallow circulating loops and deep ascending/descending loops. Along the narrow upward flow paths in the
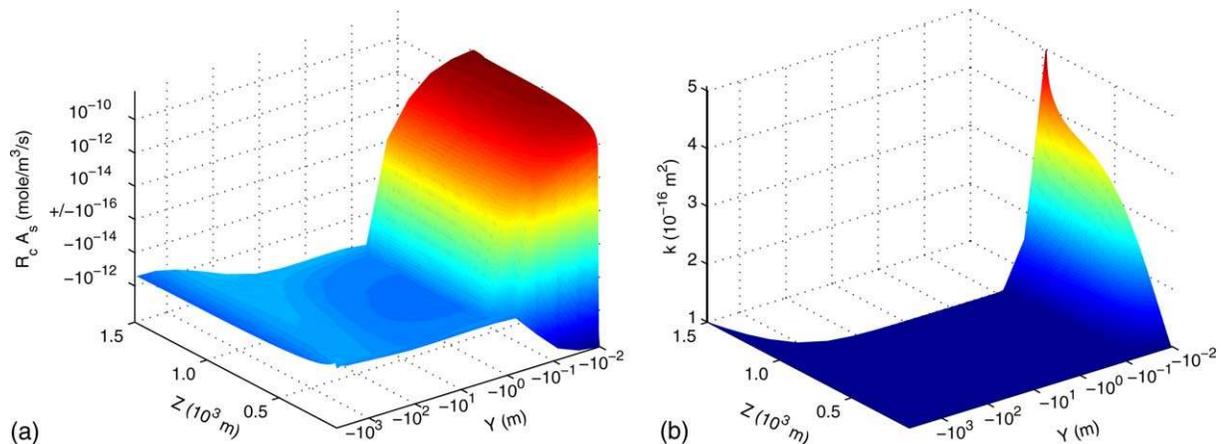
Figure 9. The alteration of permeability in the rock matrix due to dissolution/precipitation after 6300 years: (a) The dissolution rate along a vertical section ($x = 0$). Low rates of precipitation (i.e., negative rates) occur in much of the rock matrix, until the fracture is approached ($y = 0$). Very near the fracture, positive rates (i.e., dissolution) are observed. (b) Permeability field, showing that the initial rock matrix permeability is altered significantly only over a distance 10^{-1}m from the fracture.
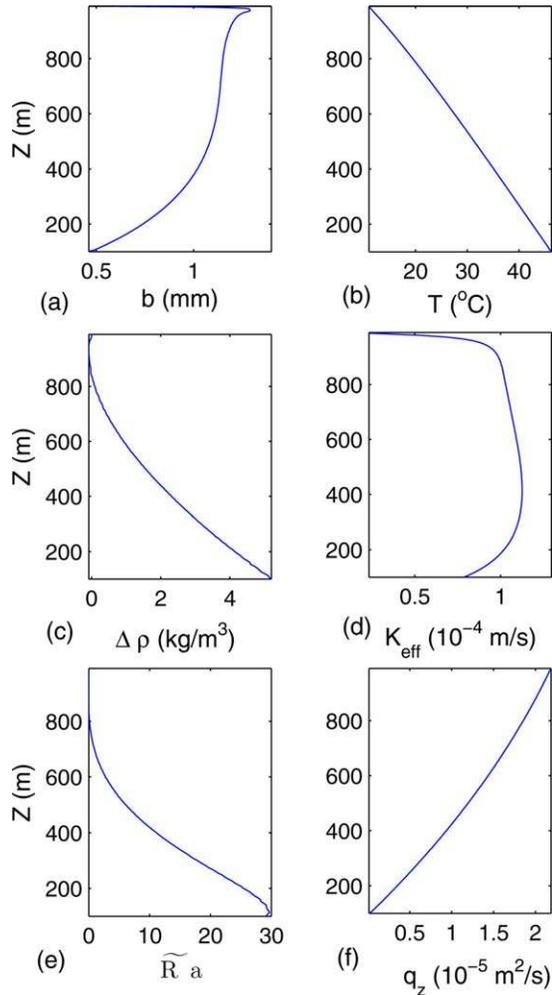
Figure 10. The vertical profiles of the horizontally averaged (a) aperture, (b) temperature, (c) density difference from the top, (d) effective hydraulic conductivity, (e) rescaled Rayleigh number, and (f) averaged-averaged upward seepage flux in the fracture; at the onset of buoyant convection for the homogeneous initial aperture field case.

double rolls, water at significantly warm temperatures is brought to the surface, and cools regardless of the vertical flow direction in the shallow circulating loops on either side (see the temperature field in Figure 7). In these shallow circulation zones, there is significant mixing between cold and warm water, and high rates of dissolution result both due to the retrograde solubility and "mixing corrosion" effects. In the dominant upward flow channels, both kinetic dissolution and dissolution due to retrograde solubility prevail. Undersaturated water flows upward, and oversaturated water flows downward along the narrow downward flow paths (see the concentration field in Figure 7). High dissolution rates in the upward flow paths and high precipitation rates in the downward flow paths are observed at this stage (see the reaction rate field in Figure 7). There is very little change in the total outflow (Figure 18a) over the entire duration of the simulation. Yet, karstification in the shallow circulation zones (< 200 m depth) is sustained by the delivery of warm water from great depths that cools within these zones and sustains high rates of dissolution. These regions

provide favorable conditions for hypogene caves and hot spring systems to develop, as in the thermal spring of Budapest [*Palmer*, 1991; *Ford and Williams*, 2007]. The porosity and permeability of the porous rock matrix do not change significantly because of precipitation in the descending flow regions due to the small fluxes (Figure 9). However, in the vicinity of the fracture where water is flowing slightly upward, dissolution occurs at low rates. The reaction rate increases rapidly as the fracture-matrix interface is approached from the rock matrix side. Even though the magnitude of dissolution rate is extremely small, the permeability grows by a factor of about 5 in 10,000 years near the fracture-rock matrix interface (Figure 9b).

[42] The geothermal power output from the hot spring is shown in Figure 18b. In the conductive and force convective heat transfer regimes (i.e., before 7000 years), the power output is nearly constant. However, after the buoyant convection is well established, there is a rapid increase in the power output until the stage when the upward flow channels become quite narrow. After approximately 9500 years, the output energy flux does not increase any more. In the later stages of the simulation, small fluctuations in the power output are observed as the permeability field keeps evolving in time. Similar fluctuations in the maximum discharge temperature were reported by *Lopez and Smith* [1995] for large fault permeability (*Lopez and Smith* [1995], Figure 10). Our simulation replicates a similar behavior as the permeability increases with time. Hence, the fluctuations in power output in Figure 18b may be considered realistic, and attributable to an unsteady convection regime. The highly nonuniform permeability field resulting from alteration may further accentuate these fluctuations.

4.1.1. Stability

[43] The transition to buoyant convection due to flow and thermal instability in the above simulations results from aperture and permeability growth [*Chaudhuri et al.*, 2009]. The lateral heat exchange between the fracture and rock matrix strongly influences thermal instability within a vertical fracture with no lateral inflow [*Murphy*, 1979; *Wang et al.*, 1987; *Tournier et al.*, 2000]. The influence of lateral heat exchange on the critical Rayleigh number was discussed by *Murphy* [1979] for both spontaneous and delayed instabilities. *Murphy* [1979] noted that for infinite thickness of the rock blocks adjacent to the fracture, the rock behaves as an insulated side wall at very late times, because the rock temperature gradient at the interface becomes very close to zero. In such cases, the critical Rayleigh number for delayed instability is the same as that for a 2-D porous medium, and equal to a constant value ($4\pi^2$). However, *Murphy* [1979] also showed that spontaneous instabilities could occur when the thermal interactions with the rock matrix are still in a transient regime. In this instability mechanism, the critical Rayleigh number is proportional to $(H/b)^2$, as the rock behaves more like a perfectly conductive wall at early times. For finite thickness of the rock matrix, *Wang et al.* [1987] formulated an intermediate scaling relationship for the critical Rayleigh number based on an asymptotic analysis. The numerical simulation results of *Tournier et al.* [2000] and *Chaudhuri et al.* [2009] satisfy the scaling relationship of *Wang et al.* [1987]. The theoretical expressions of *Wang et al.* [1987] for the critical
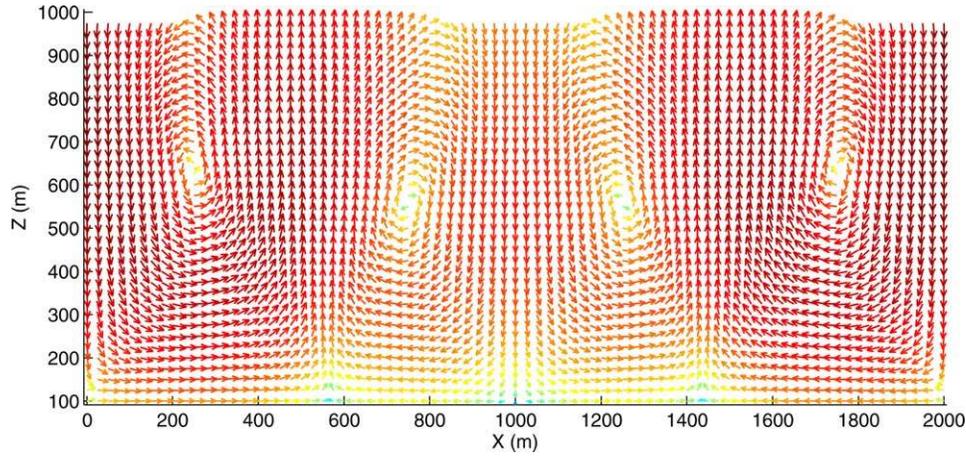
Figure 11. Initially homogeneous aperture field case: aperture-integrated water flux vector field $\mathbf{Q}_f$ at the onset of buoyant convection after eliminating the mean flow component to better illustrate the size of the convection rolls.

Rayleigh number were derived for a vertical fracture with uniform aperture, and do not incorporate aperture growth and resulting nonuniformities. When dissolution and precipitation occur, the aperture field at the onset of buoyant convection is no longer uniform. Furthermore, even if the aperture is averaged across the y-direction (see Figure 1), the averaged aperture varies along the z-direction. The nonuniform vertical aperture profile at time $t = 7132$ years is shown in Figure 10a. The vertical temperature profile is also not linear due to convective heat transport effects, especially near the outflow boundary (see Figure 10b). *Chaudhuri et al.* [2009] proposed the following expression to calculate the in situ Rayleigh number (which varies with z) for nonuniform aperture fields:

$$\text{Ra}\,(z,t) = \frac{K_{\text{eff}}\,(z,t)\Delta\rho(z,t)(H-z)}{\rho_0\kappa} \qquad (26)$$

where ρ_0 is the reference density of the water and the density difference that controls instability across the height $H - z$ is defined as $\Delta\rho(z,t) = \rho(H,t) - \rho(z,t)$. Here H denotes the height of the vertical fracture and κ is the thermal diffusivity, which is defined as $\lambda_f/(\rho C_p)_f)$. The effective hydraulic conductivity, $K_{\text{eff}}\,(z,t)$, is computed as the harmonic average:

$$K_{\text{eff}}\,(z,t) = \left(\frac{1}{H-z}\int_z^H \left(\frac{b^2(z',t)g}{12\nu(z',t)F_T(z',t)}\right)^{-1}\mathrm{d}z'\right)^{-1} \qquad (27)$$

[44] The vertical variations of $\Delta\rho(z,t)$ and $K_{\text{eff}}\,(z,t)$ just before the onset of buoyant convection are shown in Figures 10c and 10d. The maximum of $K_{\text{eff}}\,(z,t)$ near $z = 400$ m, while $\Delta\rho(z,t)$ is maximum at $z = 100$. The rescaled Rayleigh number as proposed by *Chaudhuri et al.* [2009], $\tilde{\text{Ra}}(z,t) = \text{Ra}\,(z,t)\left(\overline{b}(z_{\max},t)/(H - z_{\max})\right)$ is plotted in Figure 10e. Here, $z_{\max}$ is defined as the height where $\text{Ra}\,(z,t)$ is maximum. *Chaudhuri et al.* [2009] hypothesized that the buoyant convection rolls extend from $z_{\max}$ to the surface, which was confirmed by their numerical simulation results over a wide range of parameter values. From Figure 10e, it is seen that $z_{\max} = 115$ m for the conditions of this simulation. In the simulations shown here, lateral inflow into the fracture further modifies the situation considered by *Chaudhuri et al.* [2009]. Despite this difference, the buoyant convection rolls in Figure 6 are consistent with the analysis of *Chaudhuri et al.* [2009] in that they cover almost the entire height of the fracture, extending upward from $z \approx 100$m to the top of the domain. This becomes clearer when the velocity vectors are plotted after eliminating the mean vertical velocity profile in Figure 10f. Figure 11 shows four elliptic rolls. The elliptic shape of the rolls is also caused by lateral heat exchange with the rock, as shown by *Murphy* [1979]. The maximum value of the in situ Rayleigh number at the onset of buoyant convection is 30, which is close to the rescaled critical Rayleigh number for fracture flow bounded by a thermally conductive finite-
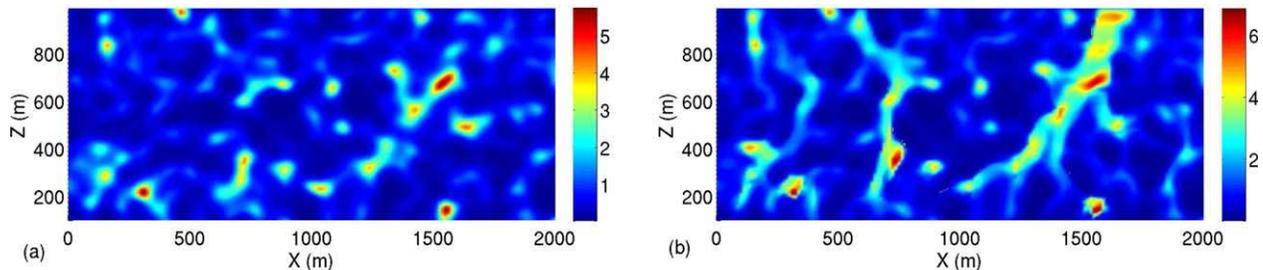
Figure 12. Evolution of the aperture field for heterogeneous initial aperture field Case 1: (a) initial aperture field and (b) aperture field after 3700 years.
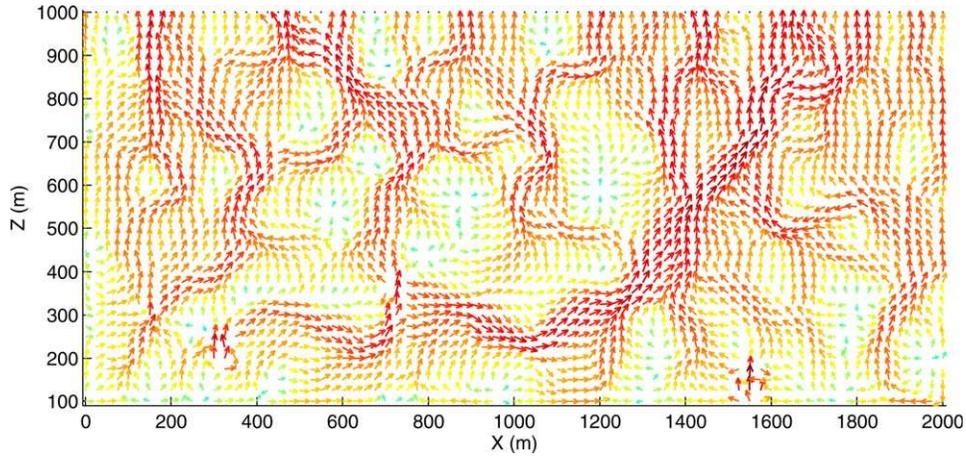
Figure 13. Heterogeneous initial aperture field Case 1: initial aperture-integrated water flux vector field $\mathbf{Q}_f$ (magnitude is in log scale).

thickness rock matrix and no lateral inflow [*Chaudhuri et al.*, 2009].

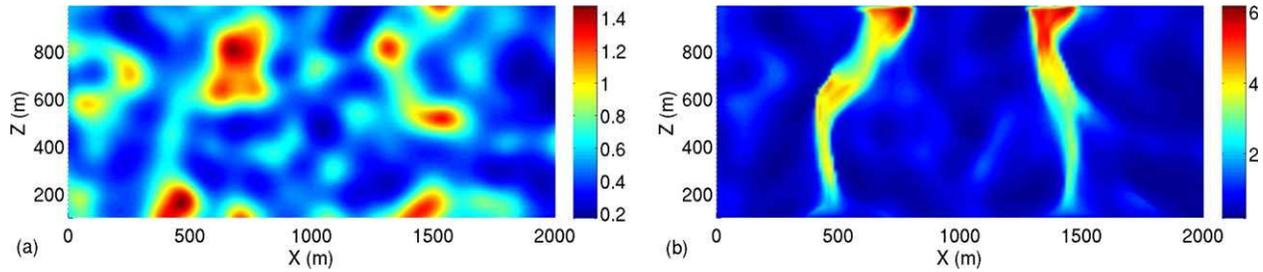### 4.2. Heterogeneous Initial Aperture Field

[45] The initial aperture fields generated using the correlation function 1 for the two simulations are shown, respectively, in Figures 12a and 15a. The effect of correlation lengths is evident from the figures as the size of large aperture patches for Case 1 (as indicated by red patches in Figure 12a) are smaller compared with Case 2. For these cases, Figures 13 and 16 show vector plots of the aperture-integrated flux at time $t = 200$ days. During the initial 200 days, there is insignificant alteration of the aperture field, and the initial transients in the flow and heat transport are dissipated, producing the quasi–steady state behavior shown in Figures 13 and 16. In both cases, the heterogeneous flow fields exhibit preferential flow channels that connect the large aperture patches. The preferential flow channels are narrower in Case 1, compared with Case 2. With time, the aperture within these preferential flow channels grows faster than in the surrounding regions, and buoyant convection effects also emerge. As noted previously, the numerical simulations in initially heterogeneous

permeability fields are rather time consuming, and for practical reasons, the simulations were executed for a run time of 45 days each (on an Intel Xeon E5620 processor). The corresponding physical time durations simulated were $t = 3700$ years for Case 1, and $t = 7260$ years for Case 2. The smaller physical time simulated for Case 1 is due to the larger degree of heterogeneity, which slows down the solver convergence to a greater extent. In both cases, buoyant convection rolls develop within the duration simulated. Buoyant convection is initiated much earlier in the heterogeneous aperture field cases because of the faster permeability growth. The onset of buoyant convection in heterogeneous permeability fields cannot be related to stability criteria in a straightforward manner, due to the complications resulting from heterogeneity and preferential flow. Thus, we did not try to analyze the behavior at the onset of instability in detail, as in subsection 4.1.

[46] In Case 1, the establishment of connectivity between large-aperture patches in the initial aperture field by preferential flow and dissolution is evident by comparing Figures 12a and 12b. Three dominant flow paths are evident at $t = 3700$ years (Figure 14). A large number of small buoyant convection cells develop within large-aperture patches.
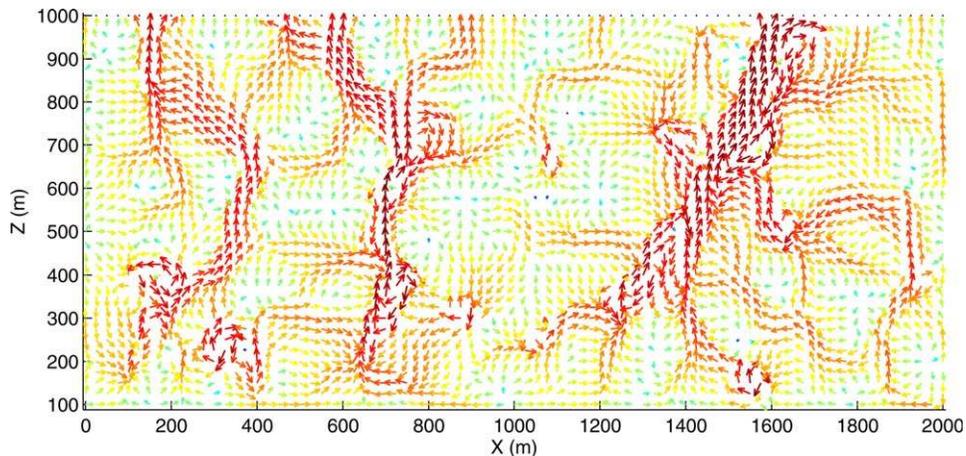
Figure 14. Heterogeneous initial aperture field Case 1: aperture-integrated water flux vector field $\mathbf{Q}_f$ (magnitude is in log scale) after 3700 years.

Figure 15. Evolution of the aperture field for heterogeneous initial aperture field Case 2: (a) initial aperture field and (b) aperture field after 7260 years.

Complex multiple interacting convection rolls are evident in the two dominant flow paths to the right, which are influenced by both forced-convective preferential flow and buoyant convection. The dominant flow path on the left (outflow at $x \approx 150$m) appears to be fed largely by forced-convective preferential flow. Case 2 with a lower degree of heterogeneity and longer correlation lengths resembles the behavior in the initially homogeneous case (section 4.1) to some extent. Two major flow paths are evident at $t = 7260$ years, both of which incorporate slender buoyant convection rolls similar to the double roll structure seen in the initially homogeneous case (Figure 8). However, unlike in the initially homogeneous case, where all the flow outside the major buoyant convection rolls is descending and supplying them with large volumes of flow; the heterogeneous Case 2 exhibits upward flow outside the buoyant convection rolls along most of the outflow boundary. As a result, less flow is supplied to the dominant flow paths compared with the homogeneous case.

[47] For all cases simulated, the changes in mass outflow with time are negligible (Figure 18a). This is largely because the overall effective permeability in this mountain hydrologic system is controlled by the low permeability of the rock matrix. Because the rock matrix permeability is not significantly altered (due to the low fluxes), the overall mass outflow remains more or less constant. However, Figure 18a shows that the thermal power output increases with time in all cases simulated. The thermal power output increases most rapidly for heterogeneous Case 1, due to

rapid enlargement of preferential flow paths in the early stages. However, the maximum value attained is lowest for this case, because the buoyant convection rolls are smaller compared with the other two cases. The power output for heterogeneous Case 2 exhibits a behavior in-between that observed for the initially homogeneous case and heterogeneous Case 1. In both initially heterogeneous cases, the rate of growth of the power output is larger than in the initially homogeneous case at early time, but the maximum power output is significantly smaller. The higher maximum power output in the initially homogeneous case owes to the formation of deep well-organized buoyant convection rolls. The power output in all cases decreases with time after it attains a maximum. This is likely due to the heat loss to the rock from the buoyant convection rolls and the progressive narrowing of the upward flow channels.

5. Summary and Discussion

[48] In this paper, we have presented a thermohydro-chemical model to represent the early stages of hypogene/thermal karstification in a simplified mountain hydrologic system that incorporates generic features of hypogene karst and thermal springs reported or summarized in previous work [*Ford and Williams*, 2007; *Perry et al.*, 1979; *Hobba et al.*, 1979; *Severini and Huntley*, 1983; *Bakalowicz et al.*, 1987; *Palmer*, 1991; *Klimchouk*, 2009; *Goldscheider et al.*, 2010; *Davidson et al.*, 2011]. In the mountain hydrologic system considered, the water table elevation is
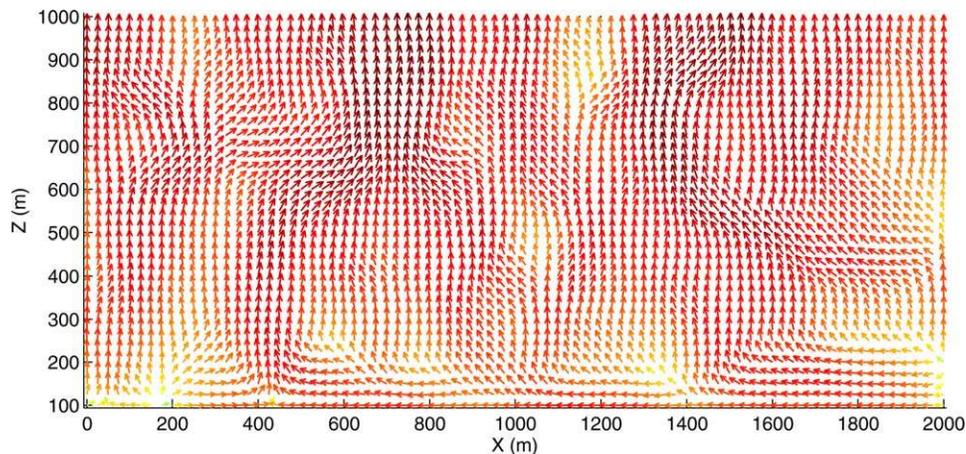
Figure 16. Heterogeneous initial aperture field Case 2: initial aperture-integrated water flux vector field $\mathbf{Q}_f$ (magnitude is in log scale).
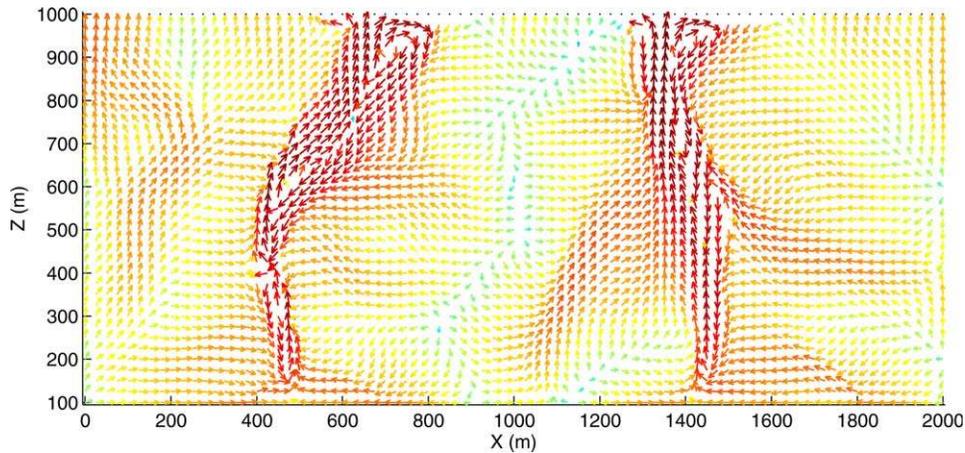
Figure 17. Heterogeneous initial aperture field Case 2: the aperture-integrated water flux vector field $\mathbf{Q}_f$ (magnitude is in log scale) after 7260 years.

prescribed in the recharge zones on the valley sides, and the discharge zone consists of an extensive vertical fracture plane. Behavior with initially homogeneous and two different types of heterogeneous (difference in spatial correlation and variance) fracture aperture/permeability fields was considered. In all the three cases simulated, the early time behavior involved a conductive heat transfer regime. In this stage, aperture growth by dissolution is largely driven by the retrograde solubility of calcite, and hence depends on the local flux and solubility gradient (related to the thermal gradient). In the case of an initially homogeneous aperture field, the aperture growth rate does not vary in the horizontal direction, but varies with elevation due to the increase in flux with elevation (as water enters from the rock matrix and flows upward through the fracture). On the other hand, in the cases with initially heterogeneous aperture fields, preferentially higher growth rates occur along high-permeability flow paths, where the local flux is larger. Buoyancy forces do not influence the flow field significantly until the overall fracture permeability becomes large enough to generate instability according to the rescaled Rayleigh number criterion in section 4.1. At this stage, buoyant convection is initiated. Late-time behavior in the case with initially homogeneous aperture field is dominated by buoyant convection, whereas in the cases with initially heterogeneous aperture fields, both preferential flow and buoyant convection, coexist and control the overall behavior. One of the key features revealed by our simulations is that buoyant convection is very likely to occur once aperture growth in the conductive heat transfer regime produces high-permeability pathways. Although the pattern of buoyant convection rolls is very organized and symmetric in the simulations with initially homogeneous aperture field, the behavior in the cases with initially heterogeneous aperture fields is much more complex, with a greater propensity for smaller localized convection rolls as the degree of heterogeneity increases. Our simulation results thus confirm *Klimchouk's* [2009] interpretation that several features in hypogene karst systems derive from buoyant convection. The localized rather than diffuse output of warm waters in the discharge zone in our simulation results is consistent with numerous observations of thermal karst springs. Our simulations suggest that the geometry of buoyant convection and heterogeneous permeability can both contribute to such localization. In all cases considered, high dissolution rates occur near the outflow boundary at relatively shallow depths, suggesting favorable conditions for hypogene cave systems to develop. Both preferential flow and buoyant convection are effective in delivering warm water to these shallow depths, where high dissolution rates are a result of both retrograde solubility (the water cools along upward flow paths) and mixing corrosion effects (interaction with shallow circulating buoyant convection). Deep buoyant convection rolls (initially homogeneous aperture case and initially heterogeneous aperture Case 2) appear to be more effective in producing large dissolution rates, compared with preferential flow. In the case with more heterogeneous initial aperture field (Case 1), smaller localized buoyant convection rolls form at greater depths along the preferential flow path, and high dissolution rates occur within these rolls. Specifically, high dissolution rates occur at multiple locations at multiple depths.

[49] In this attempt to model coupled processes operating during the early stages of hypogene karstification, we based our conceptual model on a simple mountain hydrologic system, following some of the previous studies noted above. However, we did not consider some other geologic and hydrogeologic features representative of other reported hypogene karst systems, such as mixed lithologies [e.g., *Hobba et al.*, 1979, *Ford and Williams*, 2007, *Klimchouk*, 2009] and cross-formational flow systems [*Klimchouk*, 2009], which produce transverse speleogenesis in the sense of *Klimchouk* [2003]. To some extent, this was influenced by the computationally intensive nature of the simulations, which restricted the scope of our study. Nevertheless, we note that our simulations provide several useful insights on mechanisms of early-stage speleogenesis. For instance, the dissolution growth patterns in the fracture plane do not show the formation of fingers and unstable growth by positive feedback, as noted in previous modeling studies of epigenic systems [e.g., *Hanna and Rajaram*, 1998; *Siemers and Dreybrodt*, 1998; *Szymczak and Ladd*, 2012]. Correspondingly, the generation of branch work patterns evident in fracture plane models of epigenic systems after
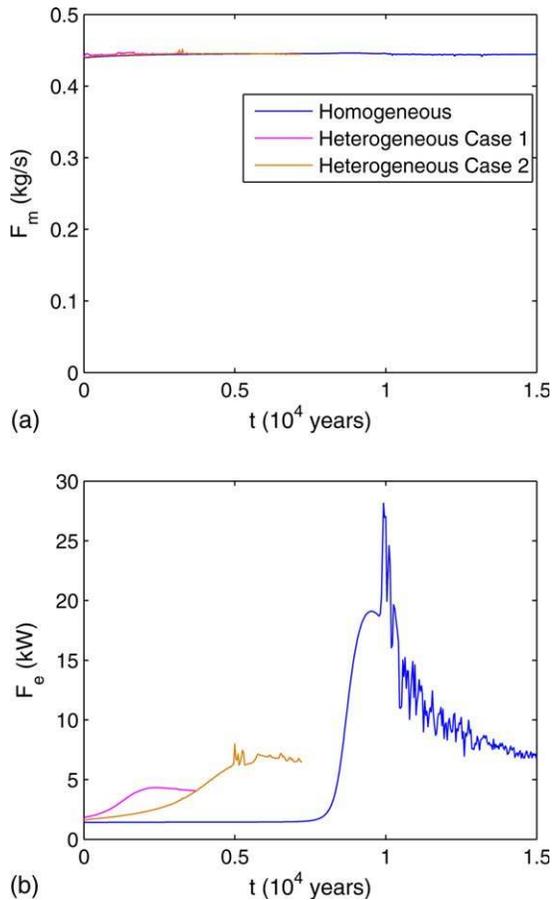
Figure 18. Variation of mass and energy flux out of the fracture with time as the aperture grows and heat transfer regime changes: (a) mass flux and (b) energy flux, shown for all cases.

breakthrough and the transition to turbulence [*Rajaram et al.*, 2009] is not expected under hypogene conditions, which is consistent with observations [*Klimchouk*, 2009]. There are two main reasons for this behavior: (i) the retrograde solubility of calcite, which maintains dissolution aggressiveness in upward flow across a geothermal gradient, and (ii) the overall flux through the system is limited by the low permeability of the rock matrix on the mountainsides, which inhibits the positive feedback the generates dissolution fingers. Within the framework of the conceptual model employed here, we are unable to demonstrate maze-like macromorphologies of hypogene systems, which largely derive from the topology of fracture networks hosting them [*Klimchouk*, 2009]; this is a fruitful avenue for future research. However, our simulations do produce features similar to several mesomorphological features characteristic of hypogene karst systems, including the "morphological suite of rising flow" described by *Klimchouk* [2009], albeit in a 2-D sense. For instance, Figures 12, 14, 15, and 17 clearly show feeder sections, through each of which flow ascends to produce transitional features that include localized buoyant convection cells, and outlet features involving buoyant convection cells; similar to the schematic description in Figure 8 of *Klimchouk* [2009]. Because our simulations focused on a single fracture plane,

the behavior reproduces mesomorphological rather than macromorphological (i.e., maze-like) features. It may also be the case that advanced mesomorphological features within hypogene cave passages involve complex 3-D flows, with secondary flows across the passage cross sections, which are not captured by aperture-averaged flow and transport equations. The role of retrograde solubility as identified in this and previous studies may also be relevant to karstification in carbonate platforms [e.g., *Moore et al.*, 2009; *Gulley et al.*, 2013b].

[50] For the mountain hydrologic system model considered here, the onset of buoyant convection occurs over timescales of the order of a few (initially heterogeneous cases) to several (initially homogeneous case) thousand years. Our simulations were run out only to 4000 to 15,000 years, during which time the initial fracture apertures enlarged by a factor of approximately 10. As aperture growth continues further to evolve large passages and eventually caves, further evolution of the geometry of buoyant convection rolls is likely, and may influence the morphology of conduit and cave systems. The results presented in this paper do not address the behavior over these longer timescales. It should be noted again that coupled thermohydrochemical model simulations are very time consuming due to the strong coupling between fluid flow and heat transfer, especially once buoyant convection effects are established. The FEHM simulations presented here each required 45 days of run time in a contemporary serial computing environment. With more advanced computational algorithms and parallel computing, it may be possible to explore behavior over much longer timescales in significantly more complex geometries. For instance, we represented the rock on the valley slopes as an equivalent porous matrix. Representation of discrete fractures within these regions could lead to more focused and localized inputs of water into the main fracture that serves as the discharge zone. In the mixing zones that develop as a result, retrograde solubility and mixing corrosion effects could combine to produce favorable conditions for karstification. As noted previously, the assumption of saturation with respect to calcite at the water table is restrictive in this context. The influence of mixing corrosion may be reduced if shallow circulating groundwater is supersaturated. The representation of the main fracture as a single vertical plane is also an idealization, and representation of a fracture zone with discrete fractures could produce more complex maze-like structures characteristic of hypogene cave systems. The representation of the central fracture zone with a network of fractures may also result in longer timescales for onset of buoyant convection, since flow will be distributed among multiple fractures, thus slowing down aperture growth rates. From a structural geologic perspective, a decrease in fracture permeability with depth in the main fracture zone may be expected, because of greater lithostatic stresses at depth. This was also a feature that we did not directly consider in our numerical simulations, mainly to retain simplicity in the model set-up. However, using an impermeable lower boundary for the hydrogeologic system serves the purpose of confining the flow to a limited depth range. We also did not consider mixed lithologies and cross-formational flow systems. However, we believe that our modeling approach can be extended to simulate at least 2-D

cross sections involving mixed lithologies, cross-formational flow systems, and fracture networks We believe that our simulations demonstrate the feasibility of coupling thermo-hydrochemical processes in karst systems over reasonably long timescales, and the potential of these coupled models as tools for understanding the behavior of thermal karst springs and early development of hypogene cave systems. The thermohydrochemical modeling framework is also relevant in the context of sustainable development of geothermal energy resources in carbonate aquifers [e.g., *Klimchouk*, 2007; *Goldscheider*, 2009]. In this connection, it is also interesting to note that the thermal power output in the simulations with initially homogeneous aperture fields was greater than in the simulations with initially heterogeneous aperture fields, largely because organized deep buoyant convection rolls could form in the former, whereas initial heterogeneity appears to produce a "competition" between preferential flow and organized buoyant convection.

Appendix A: Reactive Transport

[51] Solution of the reactive transport equation (equations (11) and (12)) requires the calculation of the dissolution precipitation rates R_c and R_{PWP}, the latter given by *Plummer et al.* [1978]:

$$R_{PWP} = k_1[H^+] + k_2[H_2CO_3^*] + k_3[H_2O] - k_4[Ca^{2+}][HCO_3^-] \quad (A1)$$

[52] The rate constants k_1, k_2, and k_3 in equation (A1) are temperature dependent [*Plummer et al.*, 1978] as shown in equation (A2) as functions of temperature (T in $^\circ$K)

$$\begin{aligned}
\log k_1 &= 0.198 - \frac{444}{T}, \quad \log k_2 = 2.84 - \frac{2177}{T} \\
\log k_3 &= -5.86 - \frac{317}{T} \quad \text{for } T \leq 298^\circ K, \\
\log k_3 &= -1.10 - \frac{1737}{T} \quad \text{for } T > 298^\circ K
\end{aligned} \quad (A2)$$

[53] The rate constant for the backward reaction, k_4, is calculated such that the forward and backward reactions are equal at saturation [*Appelo and Postma*, 1996]. Individual species concentrations appear in equation (A1). Calculation of R_{PWP} at any computational node in any time-step requires a speciation calculation to determine individual species concentrations. The equations that define this speciation calculation are composed of mass action laws corresponding to five equilibrium aqueous reactions, and values of three component concentrations obtained by solving transport equations (equations (11) and (12)) and using the invariant values for total charge and TOTC − TOTCa. The relevant mass action laws and their temperature-dependent equilibrium constants are as follows [*Stumm and Morgan*, 1992]:

$$K_w = [H^+] \cdot [OH^-], \quad K_1 = \frac{[H^+] \cdot [HCO_3^-]}{[H_2CO_3^*]}, \quad K_2 = \frac{[H^+] \cdot [CO_3^-]}{[HCO_3^-]},$$

$$\begin{aligned}
K_{CaHCO_3} &= \frac{[CaHCO_3^+]}{[Ca^{2+}] \cdot [HCO_3^{2-}]}, \quad K_{CaCO_3(Aq)} \\
&= \frac{[CaCO_3^*]}{[Ca^{2+}] \cdot [CO_3^{2-}]}, \quad K_{Ca} = [Ca^{2+}] \cdot [CO_3^{2-}] \quad (A3)
\end{aligned}$$

[54] The temperature-dependent empirical formulae for rate constants are as follows [*Busenberg and Plummer*, 1982]:

$$\begin{aligned}
\log K_1 &= -3.5631 \times 10^2 - 6.0904 \times 10^{-2}T + \frac{2.1834 \times 10^4}{T} \\
&\quad + 1.2683 \times 10^2 \log T - \frac{1.6849 \times 10^6}{T^2} \\
\log K_2 &= -1.0789 \times 10^2 - 3.2528 \times 10^{-2}T + \frac{5.1518 \times 10^3}{T} \\
&\quad + 3.8926 \times 10^1 \log T - \frac{5.6371 \times 10^5}{T^2} \\
\log K_{Ca} &= -1.7191 \times 10^2 - 7.7993 \times 10^{-2}T \\
&\quad + \frac{2.8393 \times 10^3}{T} + 71.595 \log T \\
\log K_{CaHCO_3} &= 1.2091 \times 10^3 + 3.1294 \times 10^{-1}T \\
&\quad + \frac{3.4765 \times 10^4}{T} - 4.7878 \times 10^2 \log T \\
\log K_{CaCO_3(Aq)} &= -1.2287 \times 10^3 - 2.9944 \times 10^{-1}T \\
&\quad + \frac{3.5512 \times 10^4}{T} + 4.8582 \times 10^2 \log T \\
\log K_w &= -2.8397 \times 10^2 - 5.0698 \times 10^{-2}T + \frac{1.3323 \times 10^4}{T} \\
&\quad + 1.0224 \times 10^2 \log T - \frac{1.1197 \times 10^6}{T^2}
\end{aligned}$$
$$(A4)$$

[55] Here the temperature is in $^\circ$K. The pressure dependence of K_{Ca} is taken from *Morel and Hering* [1993]. We briefly describe how this is incorporated into the kinetic reaction model below.

$$\begin{aligned}
\ln \frac{K_{Ca}}{K_{Ca\,0}} &= -\frac{\Delta V^0}{RT}(P - P_0) \Rightarrow \log K_{Ca} \\
&= \log K_{Ca\,0} - \frac{\Delta V^0}{\ln(10)RT}(P - P_0) \quad (A5)
\end{aligned}$$

[56] For the calcite dissolution kinetic reaction, $\Delta V^0 = -58.3 \, cm^3/mole$ and $R = 8.31 \, J/(mole \, ^\circ zK)$. The $\log K_{Ca\,0}$ is calculated from the expression given in equation (A4). It is considered as the reference value at reference pressure, $P_0 = 0.1 \, MPa$ (approximately equal to the atmospheric pressure). Since the species concentrations depend on TOTCa (and the other two component concentrations), R_{PWP} is an implicit nonlinear function of TOTCa, and the transport equations (equations (11) and (12)) are thus nonlinear. Global solution of equations (11) and (12) thus requires many iterations within a time-step, with a speciation calculation in each iteration. The backward reaction rate k_4 in equation (A1) is adjusted so that the overall reaction rate is zero at saturation, for a given temperature and pressure. The saturation concentration needs to be calculated from a second speciation calculation, where the ion product of Ca^{2+} and CO_3^{2-} concentrations is set to the solubility product. Although reactive transport models have been developed [*Hammond et al.*, 2007] that can handle multispecies transport problems on large 3-D domains, the associated computational effort is quite significant, especially when multispecies reactive transport is coupled to nonisothermal flow and medium alteration. For this reason, we attempted to develop simplified approximations to R_{PWP} as a function of temperature (T in $^\circ$C), pressure (P),
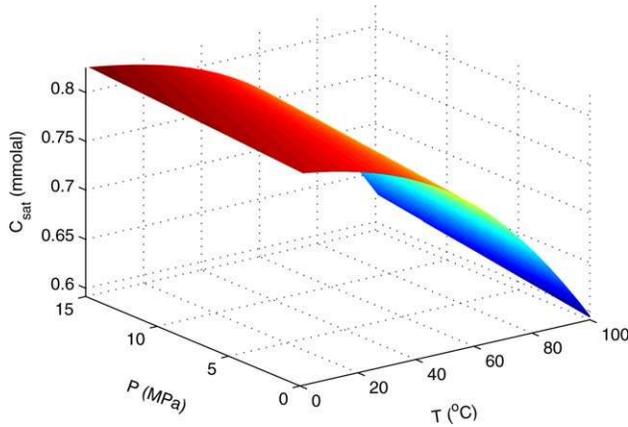
Figure A1. Equilibrium concentration of calcite as a function of temperature and pressure.

Table 1. Coefficients of the Polynomial

	$\check{C} \geq 0$
$a_0 =$	$-3.9026\text{e-}06\ P^2\ -3.8609\text{e-}04\ P\ -5.7944$
$a_1 =$	$+9.8364\text{e-}08\ P^2\ +7.6121\text{e-}06\ P\ +3.0941\text{e-}03$
$a_2 =$	$+2.3076\text{e-}05\ P^2\ +1.0917\text{e-}03\ P\ +9.9138\text{e-}01$
$a_3 =$	$+1.4111\text{e-}09\ P^2\ -6.3724\text{e-}08\ P\ +2.5441\text{e-}04$
$a_4 =$	$-1.5339\text{e-}07\ P^2\ -6.8206\text{e-}06\ P\ -1.5933\text{e-}04$
$a_5 =$	$+2.8484\text{e-}06\ P^2\ +1.3761\text{e-}04\ P\ -2.3649\text{e-}03$
$a_6 =$	$-1.6359\text{e-}11\ P^2\ +1.4434\text{e-}10\ P\ -1.4926\text{e-}06$
$a_7 =$	$+1.5301\text{e-}10\ P^2\ +9.4764\text{e-}09\ P\ +8.3051\text{e-}08$
$a_8 =$	$-9.3055\text{e-}09\ P^2\ -3.9188\text{e-}07\ P\ -1.0237\text{e-}05$
$a_9 =$	$+1.0952\text{e-}07\ P^2\ +5.4620\text{e-}06\ P\ -1.4671\text{e-}04$
	$nC \leq 0$
$a_0 =$	$+1.3576\text{e-}05\ P^2\ -6.3052\text{e-}03\ P\ -6.1682$
$a_1 =$	$-4.5738\text{e-}07\ P^2\ +1.8277\text{e-}05\ P\ +5.6209\text{e-}03$
$a_2 =$	$+3.0057\text{e-}05\ P^2\ -1.7916\text{e-}03\ P\ +8.1753\text{e-}01$
$a_3 =$	$+4.2924\text{e-}09\ P^2\ +1.5639\text{e-}07\ P\ +2.6679\text{e-}04$
$a_4 =$	$-2.7668\text{e-}07\ P^2\ -3.8176\text{e-}07\ P\ +8.5056\text{e-}04$
$a_5 =$	$+3.6752\text{e-}06\ P^2\ -2.7413\text{e-}04\ P\ -2.5308\text{e-}02$
$a_6 =$	$-1.6803\text{e-}11\ P^2\ -3.4888\text{e-}10\ P\ -1.5467\text{e-}06$
$a_7 =$	$+4.9912\text{e-}10\ P^2\ +2.7790\text{e-}08\ P\ +5.4950\text{e-}07$
$a_8 =$	$-1.5429\text{e-}08\ P^2\ +1.5612\text{e-}07\ P\ +6.3204\text{e-}05$
$a_9 =$	$+1.4055\text{e-}07\ P^2\ -1.2550\text{e-}05\ P\ -1.0651\text{e-}03$

and TOTCa. First, the saturation concentration of TOTCa (C_{sat}) was fitted as a polynomial function of T (in $^\circ$C) and P:

$$C_{\text{sat}} = 8.097 \times 10^{-4} + 1.264 \times 10^{-6}P - 6.084 \times 10^{-7}T$$
$$-4.700 \times 10^{-9}P^2 - 5.82 \times 10^{-9}PT + 1.768 \times 10^{-8}T^2 \quad \text{(A6)}$$

[57] Next, R_{PWP} was calculated for a range of values of TOTCa and T with full speciation calculations. For convenience, we use a dimensionless concentration $\tilde{C} = (C_{\text{sat}} - C)/C_{\text{sat}}$. The resulting R_{PWP} values were then fitted as functions of $\tilde{C}$, T and P with the following forms:

$$R_{\text{PWP}} = 10^r \quad \text{for} \quad \tilde{C} >= 0 \quad \text{and}$$
$$= -10^r \quad \text{for} \quad \tilde{C} <= 0 \quad \text{(A7)}$$

where $\quad r(T, \tilde{C}, P) = a_0 + a_1 T + a_2 \log|\tilde{C}| + a_3 T^2$
$+ a_4 T (\log|\tilde{C}|) + a_5 (\log|\tilde{C}|) + a_6 T^3 + a_7 T^2 (\log|\tilde{C}|) \quad \text{(A8)}$
$+ a_8 T (\log|\tilde{C}|) + a_9 (\log|\tilde{C}|)$

[58] For better accuracy, different polynomials are fitted in different ranges of $\tilde{C}$ mentioned in equation (A8). The coefficients in the above polynomial fits, which are a function of pressure, are provided in Table 1. The fitted polynomials produce the reaction rate R_{PWP} with less than 5% error when the dimensionless concentration $|\tilde{C}|$ is less than an order of 10^{-2}. When the value of $|\tilde{C}|$ is close to one, the error is approximately 10%. However, in the current setup, the $|\tilde{C}|$ is always smaller than 10^{-2}, because of the inflow boundary conditions at the water table.

[59] Using the fitted rate expressions for R_{PWP} in terms of TOTCa and T, the reactive transport equations (equations (11) and (12)) are reduced to simple nonlinear partial differential equations in a single dependent variable TOTCa, and coupled temperature and pressure fields. They can thus be solved with significantly improved efficiency using these fitted rates in place of detailed speciation calculations, without compromising accuracy.
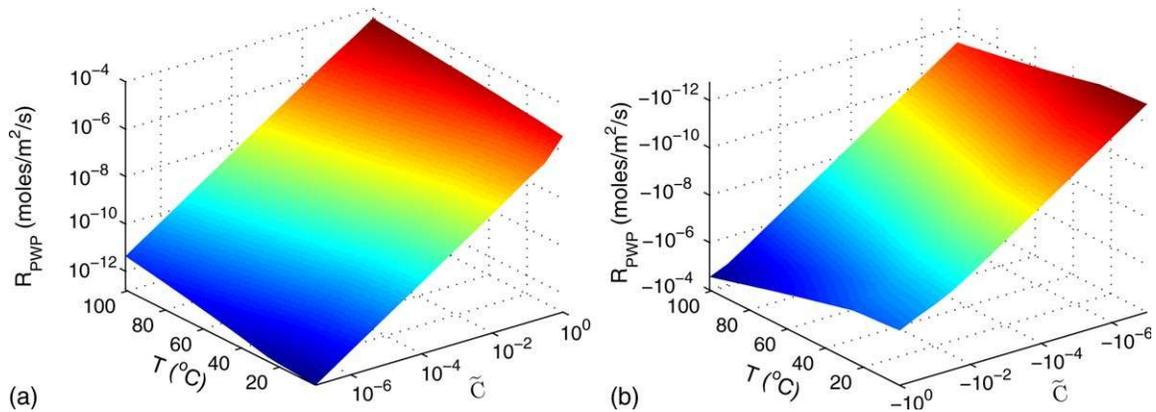
Figure A2. Variation of kinetic reaction rate with temperature and normalized calcite concentration: (a) for positive normalized concentration and (b) for negative normalized concentration.

References

Adler, P., and J. Thovert (1999), *Fractures and Fracture Networks*, Kluwer Acad., Norwell, Mass.

Andre, B. J., and H. Rajaram (2005), Dissolution of limestone fractures by cooling waters: Early development of hypogene karst systems, *Water Resour. Res.*, *41*, W01015, doi:10.1029/2004WR003331.

Andrews, J. N., W. G. Burgess, W. M. Edmunds, R. L. F. Kay, and D. J. Lee (1982), The thermal springs of Bath, *Nature*, *298*, 339–343.

Appelo, C., and D. Postma (1996), *Geochemistry, Groundwater and Pollution*, A. A. Balkema, Brookfield, Vt.

Bakalowicz M. J., D. C. Ford, T. E. Miller, A. N. Palmer, and M. V. Palmer (1987), Thermal genesis of dissolution caves in the Black Hills, South Dakota, *Geol. Soc. Am. Bull.*, *99*, 729–738.

Bear, J. (1972), *Dynamics of Fluids in Porous Media*, Dover, New York.

Bogli, A. (1964), Corrosion par melange des eaux, *Int. J. Speleogy*, *1*, 61–70.

Busenberg, E., and L. N. Plummer (1982), The kinetics of dissolution of dolomite in CO2 - H2O systems at 1.5 to 65 degrees C and O to 1 atm PCO2, *Am. J. Sci.*, *282*, 45–78.

Chaudhuri, A., H. Rajaram, and H. Viswanathan (2008), Alteration of fractures by precipitation and dissolution in gradient reaction environments: Computational results and stochastic analysis, *Water Resour. Res.*, *44*, W10410, doi:10.1029/2008WR006982.

Chaudhuri, A., H. Rajaram, H. Viswanathan, G. Zyvoloski, and P. Stauffer (2009), Buoyant convection resulting from dissolution and permeability growth in vertical limestone fractures, *Geophys. Res. Lett.*, *36*, L03401, doi:10.1029/2008GL036533.

Davidson, G. J., M. Bavea, and K. Harris (2011), Ferruginous thermal spring complexes, northwest Tasmania: Evidence that far-field stresses acting on a fracture mesh can open and maintain vertical flow in carbonate terrains, *Hydrogeol. J.*, *19*(7), 1367–1386.

Detwiler, R. L., and H. Rajaram (2007), Predicting dissolution patterns in variable aperture fractures: Development and evaluation of an enhanced depth-averaged computational model, *Water Resour. Res.*, *43*, W04403, doi:10.1029/2006WR005147.

Dreybrodt, W., and F. Gabrovsek F (2003), Basic processes and mechanisms governing the evolution of karst, *Speleogenesis Evol. Karst Aquifers*, *7*(1), 1–26.

Dreybrodt, W., F. Gabrovsek, and R. Douchko (2005), *Processes of Speleogenesis: A Modelling Approach*, Carsologica, Karst Research Institute, ZRC Postojna, Ljubljana, Slovenia.

Ford, D. C. (2006), Karst geomorphology, caves and cave deposits: A review of North American contributions during the past half century, in *Perspectives on Karst Geomorphology, Hydrology and Geochemistry: A Tribute Volume to Derek C. Ford and William B. White*, edited by R. S. Harmon and C. M. Wicks, *Geol. Soc. of America Special Paper 404*, 1–13, doi:10.1130/2006.2404(01).

Ford, D. C., and P. Williams (1989), *Karst Geomorphology and Hydrology*, 320 pp., Unwin Hyman, Winchester, Mass.

Ford, D., and P. Williams (2007), *Karst Hydrogeology and Geomorphology*, 562 pp., Wiley, Chichester.

Gelhar, L. W. (1993), *Stochastic Subsurface Hydrology*, Prentice-Hall, Upper Saddle River, N.J.

Goldscheider, N., J. Mdl-Szyni, A. Erss, and E. Schill (2010), Review: Thermal water resources in carbonate rock aquifers, *Hydrogeol. J.*, *18*, 1303–1318.

Gulley, J. D., J. M. Martin, P. J Moore, and J. Murpy (2013a), Formation of phreatic caves in an eogenetic karst aquifer by CO2 enrichment at lower water tables and subsequent flooding by sea level rise, *Earth Surf. Processes Landforms*, *38*(11), 1210–1224. doi:10.1002/esp.3358.

Gulley, J. D., J. M. Martin, P. D. Spellman, P. J. Moore, E. J. Screaton (2013b), Influence of partial confinement and Holocene river formation on groundwater flow and dissolution in the Florida carbonate platform, *Hydrol. Processes*, doi:10.1002/hyp.9601.

Hammond, G., P. Lichtner, and C. Lu (2007), Subsurface multiphase flow and multicomponent reactive transport modeling using high-performance computing, *J. Phys. Conf. Ser.*, *78*, 1–10. doi:10.1088/1742–6596/78/1/012025

Hanna, R. B., and H. Rajaram (1998), Influence of aperture variability on dissolutional growth of fissures in karst formations, *Water Resour. Res.*, *34*, 2843–2853.

Hobba, W. A. (1979), *Hydrology and Geochemistry of Thermal Springs of the Appalachians*, Washington, D.C., U.S. Govt. Print. Off.

Jones, G. D., and Y. Xiao (2006), Geothermal convection in the Tengiz carbonate platform, Kazakhstan: Reactive transport models of diagenesis and reservoir quality, *AAPG Bull.*, *90*(8), 1251–1272.

Klimchouk, A. B. (2003), Conceptualisation of speleogenesis in multi-storey artesian systems: A model of transverse speleogenesis, *Speleogenesis and Evolution of Karst Aquifers*, *1*(2). [Available at www.speleogenesis.info, 18 pp., http://www.speleogenesis.info/ archive/ publication.php?PubID=24 Type=publication.]

Klimchouk, A. B. (2007), Hypogene Speleogenesis: Hydrogeological and Morphogenetic Perspective, *NCKRI Special Paper 1*, p. 106, National Cave and Karst Research Institute, Carlsbad, N.M.

Klimchouk, A. B. (2009), Morphogenesis of hypogenic caves, *Geomorphology*, *106*, 100–117.

Koponen, A., M. Kataja, and J. Timonen (1997), Permeability and effective porosity of porous media, *Phys. Rev. E*, *56*(3), 3319–3325.

Lopez, D., and L. Smith, L. (1995), Fluid flow in fault zones: Analysis of the interplay of convective circulation and topographically driven groundwater flow, *Water Resour. Res.*, *31*(6), doi:10.1029/95WR00422.

Lopez, D., and L. Smith (1996), Fluid flow in fault zones: Influence of hydraulic anisotropy and heterogeneity on the fluid flow and heat transfer regime, *Water Resour. Res.*, *32*(10), doi:10.1029/96WR02101.

Moore P. J., J. B. Martin, and E. J. Screaton (2009), Geochemical and statistical evidence of recharge, mixing, and controls on spring discharge in an eogenetic karst aquifer, *J. Hydrol.*, *376*, 443–455.

Morel, F. M. M., and J. G. Hering (1993), *Principles and Applications of Aquatic Chemistry*, John Wiley, Hoboken, N.J.

Murphy, H. D. (1979), Convective instability in vertical fractures and faults, *J. Geophys. Res.*, *84*(11), 6121–6130.

Nield, D. A., and A. Bejan (2006), *Convection in Porous Media*, 3rd ed., Springer, New York.

Palmer, A. N. (1991), Origin and morphology of limestone caves, *Geol. Soc. Am. Bull.*, *103*, 1–21.

Palmer, A. N., and M. V. Palmer (2000), Hydrochemical interpretation of cave patterns in the Guadalupe Mountains, New Mexico, *J. Cave Karst. Stud.*, *62*, 91108.

Perry, L. D., J. K. Contain, and P. A. Geoser (1979), Heat floe in western Virginia and a model for the origin of thermal springs in the fields Appalachians, *J. Geophys. Res.*, *84*(B12), 6875–6883.

Phillips, O. M. (1991), *Flow and Reactions in Permeable Rocks*, Cambridge University Press, Cambridge.

Plummer, L. N., T. M. L. Wigley, and D. L. Parkhurst (1978), The kinetics of calcite dissolution in CO2-water systems at 5C to 60C and 0.0 to 1.0 atm CO2, *Am. J. Sci.*, *278*, 179–216.

Rajaram H., W. Cheung, and A. Chaudhuri (2009), Natural analogs for improved understanding of coupled processes in engineered earth systems: Examples from karst system evolution, *Curr. Sci.*, *97*(8), 1162–1176.

Robertson, E. C. (1988), Thermal properties of rock, *U.S. Geol. Soc. Open-File Rep. 88–441*, U.S. Geol. Surv., Reston, Va.

Robinson, B. A., H. S. Viswanathan, and A. J. Valocchi (2000), Efficient numerical techniques for modeling multicomponent ground-water transport based upon simultaneous solution of strongly coupled subsets of chemical components, *Adv. Water Resour.*, *23*, 307–324.

Svensson, U., and W. Dreybrodt (1992), Dissolution kinetics of natural calcite minerals in CO2-water systems approaching calcite equilibrium, *Chem. Geol.*, *100*, 129–145.

Severini, A. P., and D. Huntley (1983), Heat convection in warm spring, *Virginia, Ground Water*, *21*(6), 726–732.

Siemers, J., and W. Dreybrodt (1998), Early development of karst aquifers on percolation networks of fractures in limestone, *Water Resour. Res.*, *34*(3), 409–419.

Stumm, W., and J. J. Morgan (1996), *Aquatic Chemistry: Chemical Equilibria and Rates in Natural Waters*, John Wiley & Sons, N. Y.

Szymczak, P., and A. J. C. Ladd (2012), Reactive-infiltration instabilities in rocks, *Fracture dissolution, J. Fluid Mech.*, *702*, 239–264.

Tournier, C., P. Genthon, and M. Rabinowicz (2000), The onset of natural convection in vertical fault planes: Consequences for the thermal regime in crystalline basements and for heat recovery experiments, *Geophys. J. Int.*, *140*, 500–508.

Viswanathan, H. S., G. A. Zvyoloski, S. Kelkar, R. J. Pawar, A. Chaudhuri, and H. Rajaram (2009), The evolution of damage zones due to geo-mechanical and chemical effects caused by CO_2, paper presented at Eighth Annual Conference on Carbon Capture and Sequestration, Pittsburgh, PA, 4–7 May.

Wang, M., D. R. Kassoy, and P. D. Weidman (1987), Onset of convection in a vertical slab of saturated porous media between two impermeable conducting blocks, *Int. J. Heat Mass Transfer.*, *30*(7), 1331–1341.

Worthington, S. R. H., and D. C. Ford (1995), High sulfate concentrations in limestone springs: An important factor in conduit initiation?, *Environ. Geol.*, *25*, 915.

Zimmerman, R. W., A. Al-Yaarubi, C. C. Pain, and C. A. Grattoni (2004), Nonlinear regimes of fluid flow in rock fractures, *Int. J. Rock Mech. Min. Sci.*, *41*(3), 384.

Zyvoloski, G. (2007), FEHM: A control volume finite element code for simulating subsurface multi-phase multi-fluid heat and mass transfer, *Los Alamos Nat. Lab. Rep. LAUR-07-3359*, Los Alamos, N. M.